Physica Scripta

PAPER

Tailoring the physical characteristics of novel quaternary RuMnCrSi and NiMnCrAl compounds for spintronic and thermoelectric applications

RECEIVED
9 January 2025

REVISED
28 March 2025

ACCEPTED FOR PUBLICATION
1 April 2025

PUBLISHED
11 April 2025

T Ghellab[1,2], H Baaziz[1,2] and Z Charifi[1,2]

[1] Department of Physics, Faculty of Science, University of M'sila, 28000 M'sila, Algeria
[2] Laboratory of Physics and Chemistry of Materials, University of M'sila, Algeria

E-mail: baaziz_hakim@yahoo.fr and hakim.baaziz@univ-msila.dz

Keywords: half-metal characteristics, optical performance, thermoelectric applications

Abstract

In the development of advanced magneto-electronic systems, materials with high spin polarization are essential for optimizing device performance. This research explores the elastic, optical, electronic, magnetic, and thermoelectric characteristics of the Heusler alloys RuMnCrSi and NiMnCrAl. Through density functional theory (DFT) simulations, we determine that RuMnCrSi adopts a Type III crystal structure, while NiMnCrAl exhibits a Type I structure. Both structures correspond to the most stable phases for the respective alloys. The electronic properties reveal that both compounds exhibit half-metallic ferrimagnetic behavior, with RuMnCrSi showing a band gap of 0.806 eV in the majority spin channel and NiMnCrAl presenting a metallic character with no gap in the majority spin channel. The calculated total magnetic moments for RuMnCrSi and NiMnCrAl are 2 $\mu\beta$ and 1 $\mu\beta$, respectively, confirming their ferrimagnetic half-metallic nature and 100% spin polarization. Elastic constant calculations confirm the mechanical stability of both alloys, supporting their potential for practical applications. The optical properties, including the dielectric function, absorption, reflectance, and optical conductivity, were also analyzed. Both alloys demonstrate strong ultraviolet (UV) absorption, with high refractive indices, suggesting their suitability for use in spintronic devices and UV photodetectors. In the thermoelectric evaluation at 900 K, NiMnCrAl and RuMnCrSi exhibit promising performance, with ZT values of 0.3004 and 0.1977 under p-type conditions, respectively. These ZT values significantly increase to 0.6101 and 0.3583 under n-type conditions. The optimal carrier concentrations for NiMnCrAl and RuMnCrSi in p-type conditions are 0.1849×10^{20} cm^{-3} and 0.1290×10^{20} cm^{-3}, and in n-type conditions, they are -0.1421×10^{20} cm^{-3} and -0.1688×10^{20} cm^{-3}, respectively. These findings highlight the remarkable potential of RuMnCrSi and NiMnCrAl alloys in thermoelectric and spintronic applications, offering a promising avenue for next-generation energy-efficient materials and devices.

1. Introduction

Since the publication by de Groot *et al* regarding the prediction of half-metallicity in NiMnSb [1], the investigation of Heusler compounds has emerged as a prominent field of research. This specific characteristic holds potential for enhancing the efficiency of spintronics devices. Half-metals are defined as substances in which the electrons in two separate spin channels demonstrate diametrically opposed properties, thereby permitting complete spin polarisation in the vicinity of the *Fermi* level. By leveraging both charge and spin, these substances demonstrate tremendous promise for spintronics by enabling the manipulation of data storage capacity, device configuration, volatility, and dimensions. The exponential advancements in scientific research and technology have enabled the development of innovative materials with a wide range of functionalities. However, the practical implementation of these materials in spintronics technology systems is impeded by a

multitude of obstacles. The optimal choice for spintronics materials should include characteristics such as minimal flaws and disorder, significant magnetoresistance, resistance to thermal fluctuations, and a Curie temperature surpassing that of ambient conditions [2–5]. In addition, it is imperative that the suggested half-metallic compounds exhibit resemblance in crystal structure and lattice constant to semi-conductors. This similarity is crucial for enabling epitaxial growth, which in turn allows for the production of highly polarised films that are essential for spin injection into a semi-conductor. The aforementioned demanding requirements necessitate a thorough and meticulous examination, both theoretically and experimentally, of many possible candidates in order to systematically manipulate these materials for diverse purposes. In addition to Heusler alloys, Various magnetic materials, including double perovskites [6], diluted magnetic semiconductors [7, 8], manganites [9], and certain zinc-blende compounds containing transition metal elements [10], demonstrate the property of half-metallicity. Nevertheless, over the past twenty years, there has been a growing interest in Heusler alloys as a result of advancements in the understanding of structure–property relationships. These developments have enabled researchers to predict the electronic and magnetic properties of these alloys [11–13]. In addition, the Heusler compounds exhibit a notable Curie temperature [14], which positions them as viable contenders for applications at room temperature. Furthermore, their crystal structure is compatible with semiconductors, enabling efficient injection of spin-polarized current into semiconductor with a high degree of accuracy.

Heusler alloys, which are ternary intermetallics, have been the subject of substantial research due to their wide range of magnetic characteristics [15, 16]. Numerous individuals belonging to the Heusler family have been documented to exhibit a wide range of phenomena, encompassing magnetic or spin-gapless semiconductors, half-metals, and insulators. The standard notation employed to represent Heusler alloys is X_2YZ, XYZ, or XX′YZ, where X, X′, and Y represent transition metal atoms, respectively, and Z denotes an element of the main group. The compounds can exhibit several types of Heusler alloys, such as full, inverse, semi, or quaternary, depending on the configuration and quantity of elements present. All varieties of Heusler compounds exhibit a crystalline structure characterised by four interpenetrating face-centered cubic (fcc) lattices. When considering semi-Heusler compounds, it is noted that among the four sublattices that are present, one is vacant, whereas in alternative configurations, each of the four sublattices is completely occupied. Throughout our discourse, the four sublattices were identified and labelled A, B, C, and D, respectively, in accordance with their Wyckoff positions: (0,0,0), (0.25,0.25,0.25), (0.5,0.5,0.5), and (0.75,0.75,0.75). The arrangement of atoms is frequently determined by the concept of electronegativity [4]. The formation of Heusler compounds involves the selection of atoms with slight variations in electronegativity across the various sublattices. This preference can be explained by the covalent bonds that exist between the elements. Heusler compounds demonstrate a distinct atomic configuration in which the X atoms, which have a greater valence than the Y atoms, are situated in coordinates A and C. On the contrary, the Y atoms are situated in the coordinates B. Consequently, the atoms are arranged in a diagonal sequence of X-Y-X-Z. A structure endures a reduction and transforms into semi- or half-Heusler compounds when one of the positions between coordinates A and C is vacant. The inverse Heusler alloy is characterised by a distinct arrangement of X and Y atoms within the sublattices. In this structure, the valence of Y atoms exceeds that of X atoms, leading to the occupation of A and B coordinates by two X atoms, while Y atoms occupy the C coordinates. When considering the unit cell, one can witness the diagonal element arrangement as X-X-Y-Z. Upon substituting a new transition metal atom X′ for one of the two X atoms in complete Heusler alloys, a structural metamorphosis occurs, resulting in the formation of quaternary Heusler alloys. It is imperative to recognise that quaternary Heusler compounds have the standard formula XX′YZ. Nevertheless, it is important to acknowledge that the atomic arrangement along the diagonal of a unit cell conforms to the following sequence: X-Y-X′-Z. The following section will present an in-depth analysis of the three unique non-equivalent configurations of quaternary Heusler compound structures.

The potential utilisation of quaternary Heusler alloys in the field of spintronics was initially identified by Block *et al* [17, 18]. They observed a significant negative magnetoresistivity in $Co_2Cr_{0.6}Fe_{0.4}Al$ at room temperature when subjected to a weak external magnetic field. In the subsequent year, Galanakis made a prognostication on the occurrence of half-metallicity in multiple quaternary Heusler compounds [19], employing first-principles calculations. In 2009, Dai *et al* conducted a theoretical and experimental analysis of CoFeMnSi [20], which revealed a significant half-metallic gap. This finding prompted further exploration of quaternary Heusler compounds characterised by a stoichiometry of 1:1:1:1. In a subsequent study, Alijaniet *et al* expanded upon their previous research by investigating CoFeMnZ (Z = Al, Ga, Si, Ge) compounds [21]. Their findings indicated that all of these compounds exhibited characteristics of half-metallic ferromagnetism.

In a distinct study, the researchers successfully synthesised Ni-based quaternary Heusler alloys and made predictions regarding their half-metallic nature [22]. In a study conducted in 2013, Gao *et al* utilised the DFT to investigate the CoFeCr-based aloys [23]. The results demonstrated that CoFeCrSi possesses a pronounced half-metallic gap, which exhibited remarkable stability even under varying conditions. This stability was maintained when the lattice was subjected to compression, suggesting resilience to structural distortions. Furthermore, the

introduction of on-site Coulomb interactions, representing electron correlation effects, did not compromise the half-metallic nature, highlighting the robustness of the material's electronic properties under different physical influences. In a recent study, Gao *et al* conducted an investigation on a significant quantity of quaternary Heusler alloys. They employed the high-throughput DFT screening approach to analyse these compounds and successfully found 70 compounds that exhibit stability as spin gapless semiconductors (SGSs) [24]. Aull *et al* [25] utilised the dataset to detect type-I and type-II SGSs characterised by significant gaps. Additionally, they employed the information to forecast prospective candidates for reconfigurable magnetic tunnel diodes and transistors.

In this study, we investigate the transport, electronic, mechanical, and structural properties of the novel XMnCrZ compounds (where X = Ru, Ni and Z = Al, Si) using first-principles calculations combined with the BoltzTraP code. Our primary objective is to assess their potential for thermoelectric and spintronic applications by analyzing their electronic band structures, carrier transport characteristics, and mechanical stability. The computational methodology employed is detailed in section 2, followed by an in-depth discussion of the results in section 3. Finally, the conclusion presents the key findings , highlighting the most promising candidates for high-performance energy and electronic applications.

2. Computational method

The physical characteristics of the quaternary Heusler compounds XMnCrZ, where X is either Ru or Ni and Z is either Al or Si, were examined using the full potential linear augmented plane wave method. This analysis was conducted within the framework of density functional theory (DFT) [26], providing detailed insights into their electronic, magnetic, and structural properties. The WIEN2k code [27, 28] use the generalised gradient approximation (GGA) to make predictions regarding the structural, elastic, and electronic properties. The Birch-Murnaghan equation of state is commonly employed in order to ascertain structural parameters through the process of fitting the energy versus volume curve. The value of $R_{MT}K_{max}$ is selected as 9, and the Monkhorst–Pack scheme is utilised to determine the number of k-points in the *Brillouin zone*, resulting in a $15 \times 15 \times 15$ mesh [29]. The valence wave functions are enlarged up to a maximum angular momentum of $l_{max} = 10$, specifically within the atomic spheres. The potential and charge density are extended up to a maximum value of $G_{max} = 12$ atomic units per unit. To compute the second-order elastic constants (C_{ij}) and other related elastic parameters, we employed the IRELAST module [30] within the WIEN2k code. Additionally, the ElaStic code [31] was used to analyze the elastic properties of the studied compounds. ElaStic is an efficient open-source package designed to determine elastic constants through a strain-energy method. This approach involves applying a set of small deformations to the crystal lattice, computing the resulting total energies using density functional theory (DFT), and subsequently deriving the elastic constants by fitting the energy-strain relationship. The thermoelectric properties are calculated using the semiclassical BoltzTraP method [32], which is based on the rigid band approach and a constant relaxation time assumption. To enhance the accuracy of transport property calculations, a k-point mesh of 10,000 points is utilized. The cubic elastic stability is analyzed using the relaxed structure obtained through the PBE-GGA method. The Debye temperature (θ_D) and Grüneisen parameter (γ) are determined using the Gibbs2 code [33], which calculates the Gibbs free energy within the quasi-harmonic Debye model.

2.1. Structural and elastic description

The quaternary Heusler alloys RuMnCrSi and NiMnCrAl were examined in this study. These compounds have a cubic crystal structure with the space group $F\bar{4}3m$ [34, 35], as depicted in figure 1. There exist three distinct configurations of atomic sites, specifically referred to as Type-1, Type-2, and Type-3. The Wyckoff positions associated with these three configurations have been compiled and presented in table 1 [36]. To identify the most stable configuration for each compound, encompassing both magnetic (ferrimagnetic) and non-magnetic (paramagnetic) states, energy curves must be constructed, as illustrated in figure 2. The optimisation of volume for these compounds has been conducted in three different arrangements, and the resulting changes in total energy have been graphed against volume for each of the compounds under investigation. Ferrimagnetic states are exhibited by quaternary Heusler compounds across various possible configurations. The RuMnCrSi compound is classified as Type III, while NiMnCrAl falls under the Type I configuration. The derived lattice constants for the studied compounds, detailed in table 2, exhibit excellent concordance with prior computational studies [37]. The lattice parameters of the XMnCrZ quaternary Heusler alloys, with X as Ru or Ni and Z as Al or Si, align well with the theoretical predictions provided by Nepal *et al* [37]. In the ferrimagnetic phase, the bulk modulus of RuMnCrSi exhibits a higher value compared to that of NiMnCrAl. This research marks the pioneering effort to report the energy parameters V, B_0, and B' for RuMnCrSi and NiMnCrAl quaternary Heusler compounds. Notably, no prior data on the bulk modulus of these compounds has been

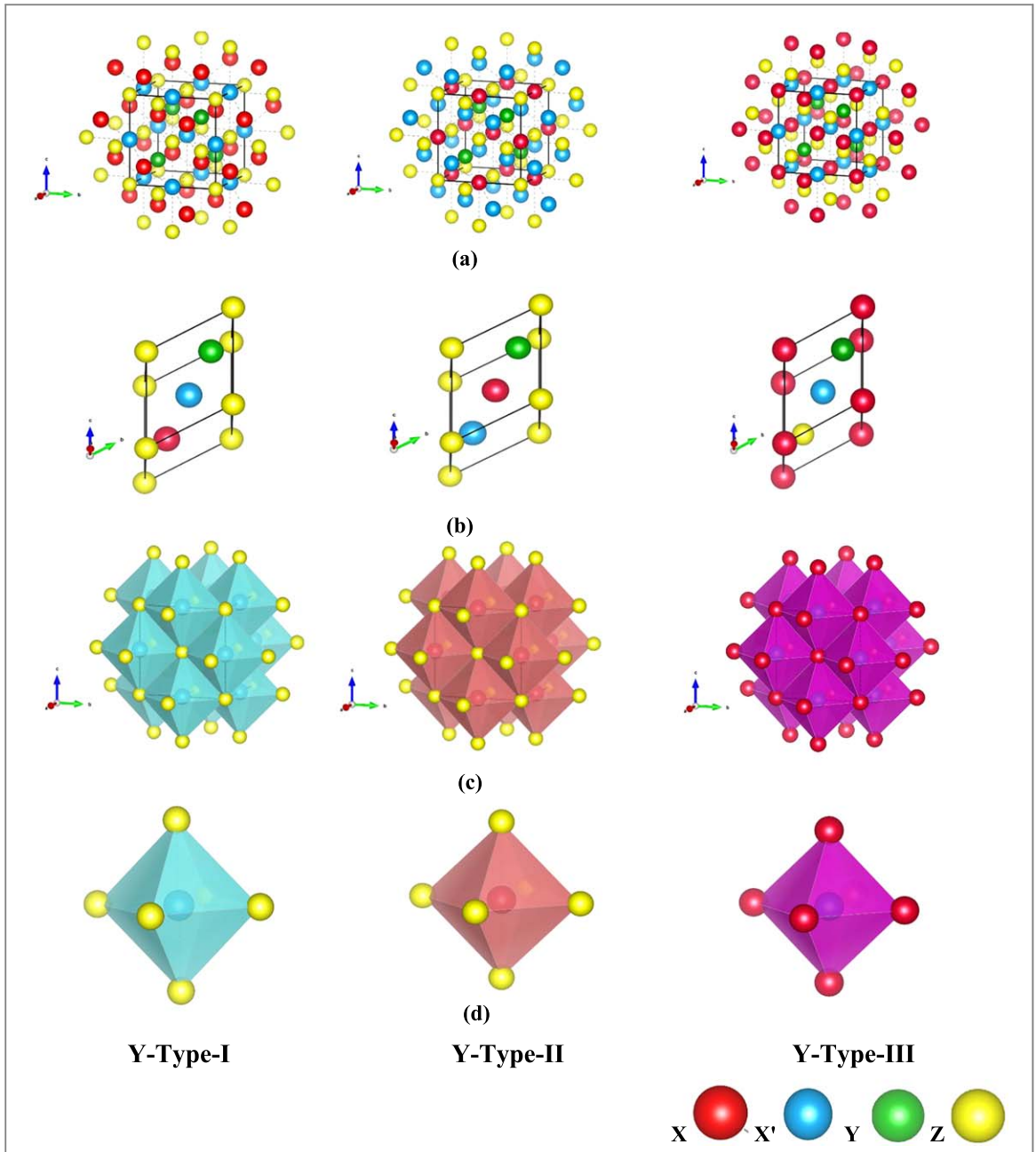

Figure 1. The three different types of cell (a) conventional in the (111) direction, (b) primitive in the $(\bar{1}11)$ direction, (c) octahedral configuration in the (111) direction, and (d) $X'Z_6$, XZ_6, $X'X_6$ octahedra in the (111) direction of Heusler quaternary compounds X X′YZ.

Table 1. The three crystal structure types of the quaternary Heusler.

Type	4a (0 , 0 , 0)	4c (1/4 , 1/4 , 1/4)	4b (1/2 , 1/2 , 1/2)	4 d (3/4 , 3/4 , 3/4)
Type I	Z = (Al, Si)	X = (Ni, Ru)	X′ = (Mn)	Y = (Cr)
Type II	Z = (Al, Si)	X′ = (Mn)	X = (Ni, Ru)	Y = (Cr)
Type III	X = (Ni, Ru)	Z = (Al, Si)	X′ = (Mn)	Y = (Cr)

published, highlighting the novelty of these results. The computational findings outlined here provide a valuable foundation for future experimental work aimed at characterizing these materials.

Cohesive and formation energies can be utilized to determine the physicochemical stability of quaternary $E_{Tot}^{XX_0YZ}$ Heusler alloys:

$$E_{For} = \frac{1}{4}[E_{Tot}^{XX_0YZ} - (E_{bulk}^{X} + E_{bulk}^{X_0} + E_{bulk}^{Y} + E_{bulk}^{Z})] \quad (1)$$

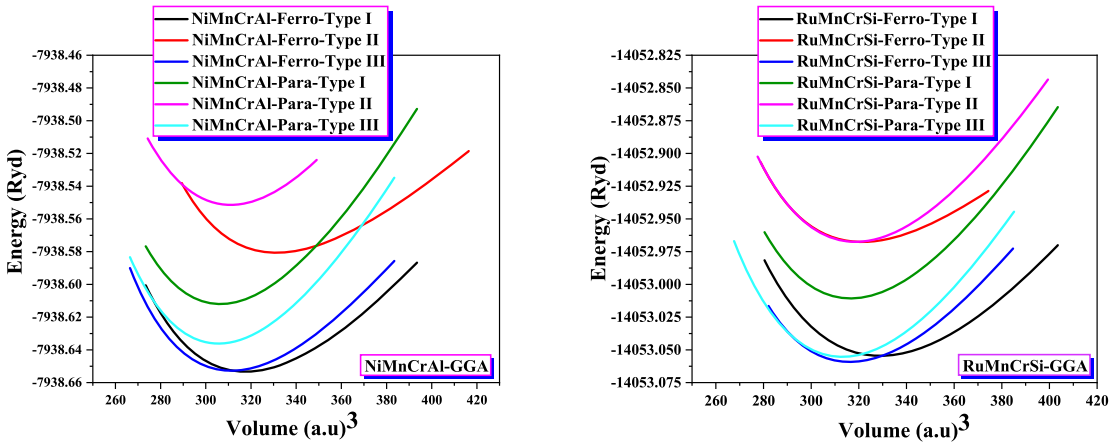

Figure 2. Energy variation with volume in the paramagnetic and ferrimagnetic states for the three types of NiMnCrAl and RuMnCrSi.

Where $E_{Tot}^{XX_0YZ}$ is the equilibrium total energy in the most stable phase for RhFeMnZ and IrMnCrZ (where Z represents Si, and Ge). E_{bulk}^{X}, $E_{bulk}^{X_0}$, E_{bulk}^{Y}, and E_{bulk}^{Z} are the equilibrium total energies per atom for bulk X = Ru/Ni, X_0 = Mn, Y = Cr, and Z = Si/Al, for RuMnCrSi and NiMnCrAl, respectively. The computed formation energies of RuMnCrSi and NiMnCrAl provide essential insights into their thermodynamic stability and potential feasibility for experimental synthesis. The formation energy of RuMnCrSi was determined to be -2.14 eV atom^{-1}, while that of NiMnCrAl was found to be -1.90 eV atom^{-1}. The negative formation energies for both compounds indicate that their synthesis is energetically favorable, meaning they can be formed from their constituent elements without requiring excessive external energy input.

Among the two compounds, RuMnCrSi exhibits the lower (more negative) formation energy, suggesting that it is thermodynamically more stable than NiMnCrAl. This implies that RuMnCrSi may have a higher probability of forming in equilibrium conditions, making it a stronger candidate for experimental realization. The relatively lower formation energy of NiMnCrAl still confirms its stability but suggests that it may be slightly less favorable compared to RuMnCrSi.

The high stability of both compounds can be attributed to strong atomic interactions and bonding characteristics within their structures. The presence of transition metals (Ru, Ni, Mn, Cr) enhances the metallic and covalent bonding nature, while Si and Al contribute to structural integrity and electronic stability. Such thermodynamically stable configurations indicate potential applications in materials science, particularly in fields where high stability and resistance to decomposition are critical. These findings provide a strong foundation for further investigations into their structural, electronic, and magnetic properties, as well as their potential applications in functional materials and alloy design.

This section focuses on analyzing the mechanical properties of the studied compounds. The outcomes of the calculations for the elastic constants are displayed in table 3. In the context of the cubic system, there are three elastic constants that are considered to be independent, namely C_{11}, C_{12}, and C_{44}. The stability of the cubic crystal structure can be evaluated using the Born–Huang stability criteria [38], which are expressed through the following conditions:

$$C11 - C12 > 0, \quad C11 > 0, \quad C44 > 0, \quad C11 + 2 \quad C12 > 0, \quad C11 < B < C12 \tag{2}$$

Crystals that meet the aforementioned characteristics are regarded as stable.

The materials presented in table 3 adhere to the Born–Huang stability criteria, thereby confirming their mechanical stability. Insights into the mechanical durability, elasticity, and resistance to deformation of the studied materials are offered by the elastic constants. C_{44} represents the resistance of a material to deformations induced by stress, whereas C_{11} determines the rigidity of the material under the influence of applied stress [39]. The dominance of the C_{11} constant over the other values in our calculations points to the studied materials having a higher resistance to longitudinal changes than to volumetric or shape transformations. It is expected that the crystallographic direction 100 will demonstrate the greatest density. C_{11} (RuMnCrSi) is a compound with more advantageous characteristics than C_{11} (NiMnCrAl). As a result, it is evident that RuMnCrSi bonds demonstrate a greater level of rigidity along the [100] axis in comparison to NiMnCrAl bonds. Upon comparing C_{44} (NiMnCrAl) and C_{44} (NiMnCrAl), it can be inferred that NiMnCrAl demonstrates a more pronounced level of monoclinic shear deformation along the [010] axis in the (100) planes. By utilising the elastic constants, several elastic properties can be computed, including the elastic moduli such as Young's modulus (E), Shear

Table 2. The structural parameters of NiMnCrAl and RuMnCrSi were computed with the GGA approximation.

Compounds	Type	Physical parameters	Our calculations		Theoretical calculations [36]
			Para	Ferro	
NiMnCrAl	Type I	a (Å)	5.6642	5.7318	5.8250
		$(\Delta a/a)_{\text{theo}}$	−2.83%	−1.62%	—
		B (GPa)	228.5104	176.1455	—
		B'	4.7231	5.8630	—
		E_{min} (Ryd)	−7938.611953	−7938.653383	—
		Volume (u.a)^3	306.5814	317.7009	—
		M_{Tot} (μ_B)	—	1.66495	2.00
	Type II	a (Å)	5.6912	5.8160	5.9360
		$(\Delta a/a)_{\text{theo}}$	−4.30%	−2.06%	—
		B (GPa)	215.9802	153.8513	—
		B'	4.7627	6.8139	—
		E_{min} (Ryd)	−7938.551426	−7938.580597	—
		Volume (u.a)^3	310.9902	331.8998	—
		M_{Tot} (μ_B)	—	0.29867	0.27
	Type III	a (Å)	5.6589	5.6931	5.7750
		$(\Delta a/a)_{\text{theo}}$	−2.05%	−1.43%	—
		B (GPa)	233.0462	194.1594	—
		B'	4.7972	6.2016	—
		E_{min} (Ryd)	−7938.636164	−7938.652884	—
		Volume (u.a)^3	305.7276	311.2991	—
		M_{Tot} (μ_B)	—	1.58216	1.88
RuMnCrSi	Type I	a (Å)	5.7259	5.7986	5.8742
		$(\Delta a/a)_{\text{theo}}$	−2.58%	−1.30%	—
		B (GPa)	281.7993	218.1804	—
		B'	4.5440	4.8475	—
		E_{min} (Ryd)	−14053.010669	−14053.054622	—
		Volume (u.a)^3	316.7078	328.9321	—
		M_{Tot} (μ_B)	—	1.00863	1.01
	Type II	a (Å)	5.7378	5.7544	5.8540
		$(\Delta a/a)_{\text{theo}}$	−2.02%	−1.73%	—
		B (GPa)	273.7588	206.2753	—
		B'	4.7261	7.7407	—
		E_{min} (Ryd)	−14052.967515	−14052.967680	—
		Volume (u.a)^3	318.6875	321.4728	—
		M_{Tot} (μ_B)	—	3.57442	0.45
	Type III	a (Å)	5.7034	5.7232	5.7837
		$(\Delta a/a)_{\text{theo}}$	−1.40%	−1.06%	—
		B (GPa)	291.1255	263.0310	—
		B'	4.7584	5.5459	—
		E_{min} (Ryd)	−14053.055440	−14053.059284	—
		Volume (u.a)^3	312.9992	316.2639	—
		M_{Tot} (μ_B)	—	1.00802	1.01

modulus (G), and Bulk modulus (B), as well as the anisotropy factor (A_1). The aforementioned moduli are applicable for characterising polycrystalline materials whereby the crystal grains exhibit random orientation. The moduli can be assessed by taking the average of the second-order elastic compliance (S_{ij}) or elastic stiffness (C_{ij}). The Voigt-Ruess-Hill method, widely recognised in the field, is the most commonly employed technique for determining the elastic moduli of materials with polycrystalline structure [40–43]. The B values of NiMnCrAl-Type I and RuMnCrSi-Type III, which were determined under conditions of absolute zero pressure and temperature, are outlined in table 3 as 175.229 GPa and 267.194 GPa, respectively. The outputs that were observed bear a striking resemblance to those derived from the equation of state, precisely 263.0310 GPa and 176.1455, which are detailed in table 2. It has been determined that RuMnCrSi-Type III possesses greater shear and Young's moduli than NiMnCrAl-Type I. This disparity suggests that RuMnCrSi is more rigid than NiMnCrAl. The Pugh ($k = B/G$) and Poison's (σ) ratios, the values of which are provided in table 3, can be utilised to analyse the distinctive attributes of compounds, including brittleness, ductility, and malleability. The ductility and brittleness of a material can be deduced using Pugh's criterion and the critical value of Pugh's ratio, $k_c = 1{:}75$ [44–46]. At $k < k_c$, the material is brittle; at $k > k_c$, it is ductile. The material RuMnCrSi exhibits a value of k that exceeds 1.75, indicating its ductile nature. Conversely, the material NiMnCrAl displays a value of k that

Table 3. The elastic parameters, the anisotropy index, the melting temperature T_{melt}, the velocity of both the longitudinal and transverse waves ($\boldsymbol{v_t}$, $\boldsymbol{v_l}$), the mean velocity of sound ($\boldsymbol{v_m}$), and the temperature of Debye Θ_D of the quaternary Heusler compounds NiMnCrAl and RuMnCrSi.

	NiMnCrAl-Type I	RuMnCrSi-Type III
C_{11} (GPA)	262.0475	410.6179
C_{12}(GPA)	131.8208	195.4828
C_{44}(GPA)	162.2631	141.8748
B_H(GPA)	175.229	267.194
G_V(GPA)	123.402	128.151
G_R(GPA)	101.617	125.822
G_H (GPA)	112.509	126.986
E_V (GPA)	299.824	331.461
E_R (GPA)	255.468	326.254
E_H(GPA)	278.023	328.860
σ_V	0. 214	0. 293
σ_R	0. 257	0. 296
σ_H	0. 235	0. 294
A_1	2.49201	1.31894
T_{melt}(K)	2101.7007 ± 300	2979.7517 ± 300
B_H/G_H	1.55745	2.1041
A_G%	9.68168	0.916992
A^U	1.07195	0.0925479
v_t (m s^{-1})	4069.43	3896.19
v_l (m s^{-1})	6918.99	7223.68
v_m (m s^{-1})	4510.31	4349.14
Θ_D (K)	590.338	570.098

is below 1.75, signifying its fragility. This claim can be supported by examining Cauchy's Pressure equation, which is expressed as $C_p = C_{12} - C_{44}$. The ductility of a material serves as an indicator of the presence of metallic bonds, which are typically associated with greater malleability and the ability to deform under stress without fracturing. In contrast, materials that exhibit brittleness are characterized by the dominance of covalent or ionic bonds, which result in lower flexibility and a tendency to fracture under stress. Pettifor's criterion [47] provides a quantitative measure to distinguish between these bonding types. Specifically, a positive Cauchy pressure is indicative of metallic bonding, highlighting a material's ability to withstand deformation. On the other hand, a negative Cauchy pressure signifies the dominance of covalent or ionic bonds, reflecting the material's brittleness and its limited capacity to endure structural strain without breaking. This criterion offers valuable insights into the mechanical behavior of materials and their bonding nature. Consequently, substances possessing negative C_p can be deemed brittle, while those possessing positive C_p can be deemed ductile. The data presented in table 3 indicates that RuMnCrSi possesses a positive C_p value, while NiMnCrAl exhibits a negative C_p value. These results indicate that RuMnCrSi is ductile in nature, while NiMnCrAl is brittle. Our previous estimation of ductility and brittleness, which was determined by the value of Pugh's ratio (k), is confirmed by this observation. The longitudinal, transverse, and average sound velocities for the RuMnCrSi and NiMnCrAl alloys were computed, complementing the previously mentioned analyses. The data in table 3 reveal that the propagation velocity of longitudinal elastic waves exceeds that of transverse waves [48]. The Debye temperature (θ_D) has been calculated using the provided sound velocities. The Debye temperature is a key physical parameter that links a crystal's elastic constants to various properties such as specific heat capacity, thermal conductivity, and melting point. At low temperatures, the variation of second-order elastic constants with temperature offers insights into the Debye temperature (θ_D). An observation is made that the Debye temperature (θ_D) of RuMnCrSi is diminished in comparison to NiMnCrAl, which suggests the possibility of lowered thermal conductivity of the lattice. This relationship is established through the direct connection between lattice heat conductivity and the Debye temperature [49]. The melting points (T_{melt}) of the compounds RuMnCrSi and NiMnCrAl analyzed in this study are thoroughly described in table 3.

Crystallographic elastic anisotropy can greatly impact various physical phenomena, including fracture behavior, anisotropic deformation, and elastic instability. After determining the Zener parameter (A_1), the elastic anisotropy of NiMnCrAl and RuMnCrSi was further assessed using three additional techniques. The second method involves the approach described in reference [50], which assesses the degree of elastic anisotropy under shear conditions.

$$A_G = (G_V - G_R)/(G_V + G_R) \times 100 \tag{3}$$

The A_G value for materials showing isotropic properties is calculated as zero. There exists a state of elastic shear anisotropy between A_G and zero. When the A_G value hits 100 percent, it indicates the presence of the greatest potential anisotropy. The differentiation between NiMnCrAl-Type I and RuMnCrSi-Type III is mostly based on their shear anisotropy. The percentages for the respective numbers, according to the GGA, are about 9.681 and 0.916, as indicated in table 3. The NiMnCrAl-Type I material demonstrates a notable level of anisotropy in its shear modulus. The RuMnCrSi-Type III material exhibits a near-isotropic behaviour in terms of its shear modulus.

The third method involves calculating the universal index [51].

$$A^U = 5\frac{G_V}{G_R} + \frac{B_V}{B_R} - 6 \tag{4}$$

Zero is the A^U value for isotropic materials. A transition from zero to positive amplitude characterises crystallographic anisotropy. Based on the universal index A^U calculations for NiMnCrAl-Type I and RuMnCrSi-Type III utilising the GGA approximation, the results are displayed in table 3. 1.072 and 0.093 are the approximate A^U values that were acquired. Elastic anisotropy is a property similar to all compounds.

For practical applications, surface structures with directional reciprocity in Young's modulus are often preferred. Polar diagrams in three dimensions are useful for illustrating how the E modulus is distributed in a cubic system, giving a complete view of its directional dependence. The following equation, derived from Nye's work [52], describes this dependence:

$$E = \frac{1}{S_{11} - 2\left(S_{11} - S_{12} - \frac{1}{2}S_{44}\right)(n_1^2 n_2^2 + n_2^2 n_3^2 + n_3^2 n_1^2)} \tag{5}$$

The orientations along the x, y, and z axes in spherical coordinates are determined by the cosine of the angles, $n_1 = \sin\theta\cos\varphi$, $n_2 = \sin\theta\sin\varphi$, and $n_3 = \cos\theta$. This is associated with the elastic constant for deformability, denoted as S_{ij}. Figure 3 shows E for NiMnCrAl and RuMnCrSi at various orientations, calculated using the elastic compliance coefficients as a baseline.

A three-dimensional closed surface, obtained from solving equation (5), illustrates the directional Young's modulus, with the distance from the origin to the surface indicating the modulus in each direction. In an ideal isotropic structure, this surface would be spherical.

However, the Young's modulus surface of NiMnCrAl-Type I demonstrates a distinct non-spherical morphology, indicating pronounced anisotropy. This anisotropy arises from the unique bonding characteristics of neighbouring atomic planes, leading to significant differences in elastic properties between these planes. Specifically, the (X = Y) plane exhibits higher elastic anisotropy compared to the (XY), (XZ), and (YZ) planes. Conversely, the Young's modulus surface for RuMnCrSi-Type III is nearly spherical, suggesting a behaviour closer to isotropy. For this material, the (X = Y) plane exhibits more pronounced elastic isotropy than the (XY), (XZ), and (YZ) planes.

2.2. Electronic and magnetic description

'The electronic properties of RuMnCrSi and NiMnCrAl compounds are evaluated by analyzing their band structures and density of states, with PBE-GGA used to optimize the lattice parameters for the most stable configurations. The spin-polarized band structures of the Heusler Type III compound RuMnCrSi and the Type I compound NiMnCrAl were computed along high-symmetry paths in the first Brillouin zone. Notably, the GGA method used for NiMnCrAl reveals an energy gap in both spin directions. For minority spins, both the valence band maximum (VBM) and conduction band minimum (CBM) are located at the high-symmetry point Γ, indicating a direct band gap. The Fermi energy is close to the CBM, classifying the material as n-type. In contrast, for majority spins, the VBM is located at Γ, and the CBM is at the high-symmetry point X, suggesting an indirect band gap. The GGA method used for NiMnCrAl reveals an energy gap in both spin directions. For minority spins, both the valence band maximum (VBM) and conduction band minimum (CBM) are located at the high-symmetry point Γ, indicating a direct band gap. The Fermi energy is close to the CBM, classifying the material as *n*-type. In contrast, for majority spins, the VBM is located at Γ, and the CBM is at the high-symmetry point X, suggesting an indirect band gap. The compound RuMnCrSi exhibits semi-metallic behavior, specifically half-metallic properties, when analyzed using the mBJ-GGA approximation. This is attributed to the metallic character for majority spins, while minority spins display an indirect energy gap (Γ-X) of zero, indicating gapless behavior. In contrast, when the GGA approximation is employed, the compound exhibits metallic properties, as shown in figure 4. The application of the mBJ-GGA, considering the minority spin direction, reveals that the RuMnCrSi-Type III and NiMnCrAl-Type I compounds have band gaps of 0.806 eV and 0 eV, respectively, as listed in table 4, suggesting semi-metallic behavior.

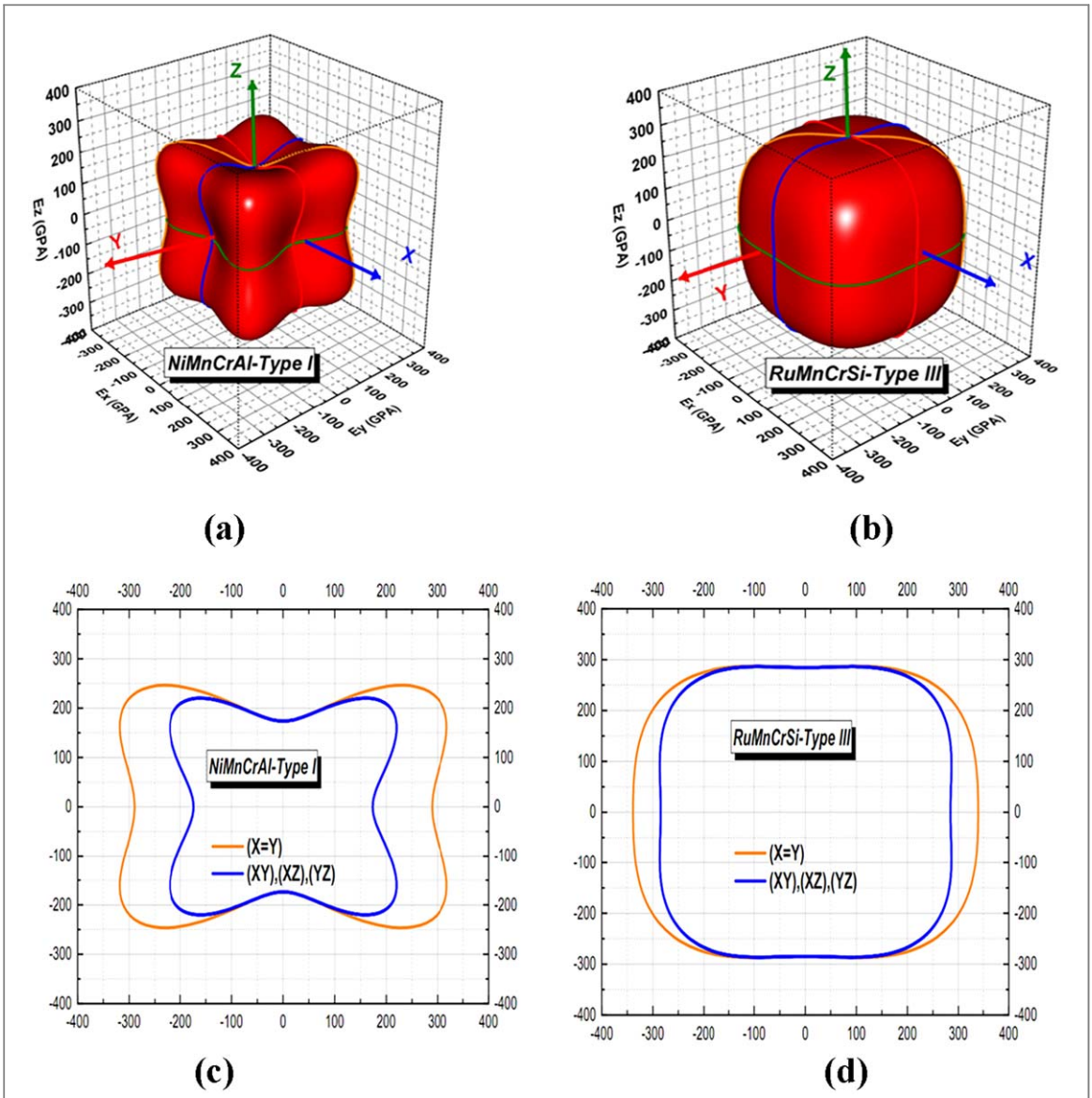

Figure 3. 3D surface plots of the Young's modulus: (a) for NiMnCrAl, (b) for RuMnCrSi, and their transverse sections in separate planes (c) and (d).

Figure 5 presents the total and partial density of states (DOS) of RuMnCrSi and NiMnCrAl, with mBJ-GGA. The curves illustrate the relationship between the number of electron states and energy. For both RuMnCrSi and NiMnCrAl, the dominant contribution to the total density of states (DOS) for majority spins below the Fermi level comes mainly from the Ni/Ru atoms, along with contributions from Mn and Cr atoms, due to their *3 d/4 d* and *3 d* electron configurations. In contrast, for minority spins, the dominant contribution below the Fermi level comes from the Ni/Ru and Mn atoms, influenced by the *3 d/4 d*, *3 d*, and *4 d* electron orbitals. Within the conduction band, the compounds show a unified contribution from the orbitals of atoms X, X0, and Y, with a negligible role played by atom Z.

The Slater-Pauling rule plays a crucial role in defining the magnetic properties of Heusler alloys by providing a method for estimating the total spin magnetic moment (M_{Tot}) from the number of valence electrons (N_v). This rule is particularly significant because it ensures that Heusler compounds follow a predictable trend, which allows for the precise calculation of the total spin magnetic moment. By adhering to the Slater-Pauling rule, these alloys maintain a well-established total spin magnetic moment that is fundamental to their magnetic behavior. This consistency is essential for the stabilization of ideal semi-metallic ferrimagnetic states or semiconductors that do not exhibit a spin gap. In these materials, the distribution of valence electrons across majority and minority spin channels plays a key role in determining the magnetic moment. The difference in electron population between the two spin states directly influences the total spin moment, highlighting the interplay between electron configuration and magnetic properties in Heusler alloys.

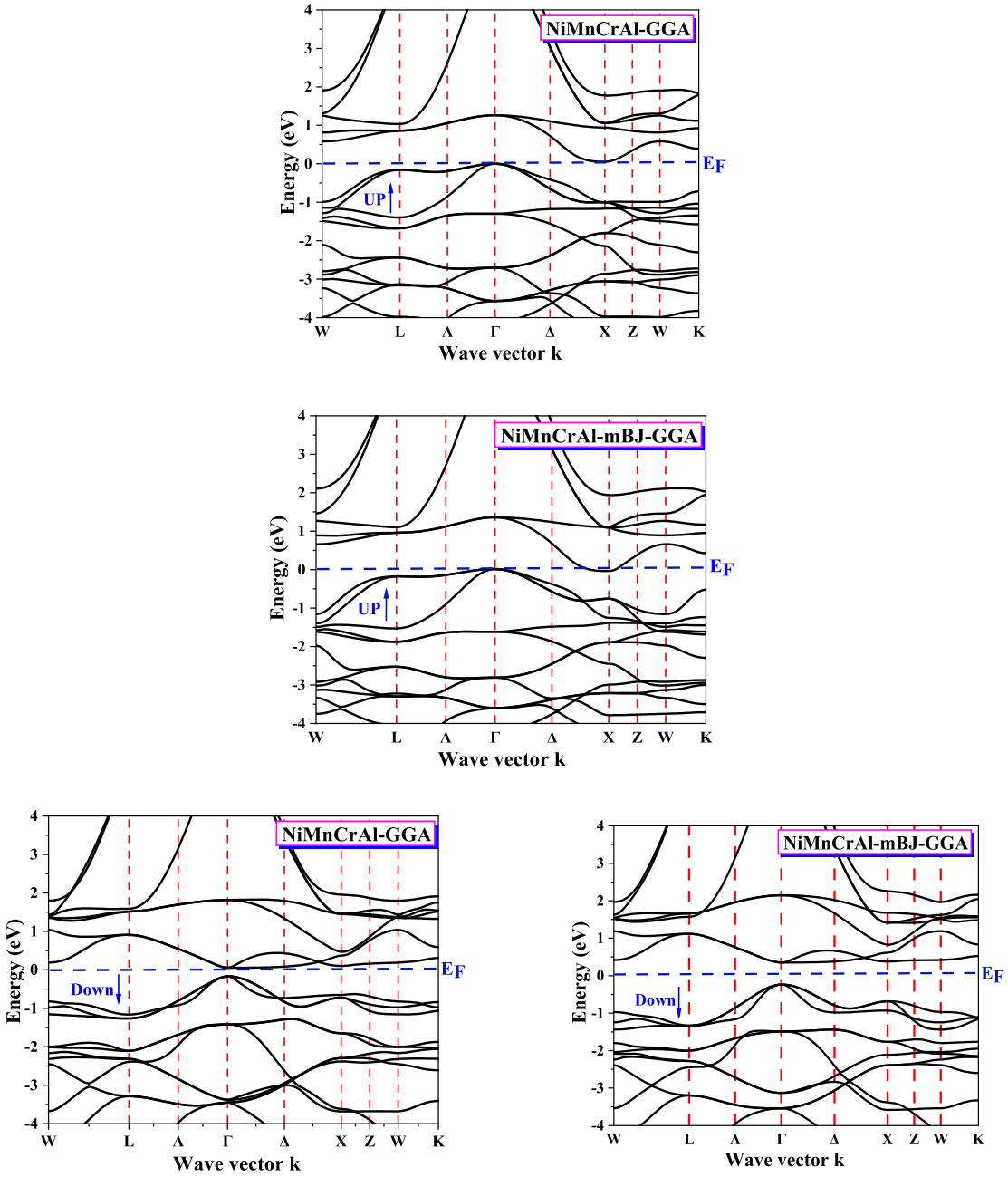

Figure 4. Band structures for spin-up (↑) and spin-down (↓) states, calculated in the most stable phase for NiMnCrAl-Type-I and RuMnCrSi-Type-III alloys with the GGA and mBJ-GGA approximations.

The positioning of Y atoms relative to X and X′ in our compounds often leads to a nuanced application of the Slater-Pauling rule. In the present study, all compounds adhere to the expression $M_{Tot} = N_v - 24$, allowing for the determination of the total spin magnetic moment (M_{Tot}) based on the number of valence electrons (N_v). The hybridization model, which has been extensively discussed in the literature [11, 53], provides a useful framework for understanding the electronic and magnetic properties of Heusler alloys [54–56]. This model is particularly effective in explaining the behaviors observed in various compounds, offering insights into the nature of their bonding and electronic structure.

In our alloys that follow the $M_{Tot} = N_v - 24$ rule, the coordination sites A and C in Type III structures exhibit distinct characteristics that influence the hybridization of the constituent atoms. Initially, the elements X and X′ undergo hybridization, which results in the formation of double ($e_{.g.}$) and triple (t_{2g}) hybrid states. The transition metal Y then interacts with these hybridized orbitals, leading to the creation of five bonding states, five anti-bonding states, and five non-bonding states. This arrangement significantly affects the electronic structure and, consequently, the magnetic properties of the compound.

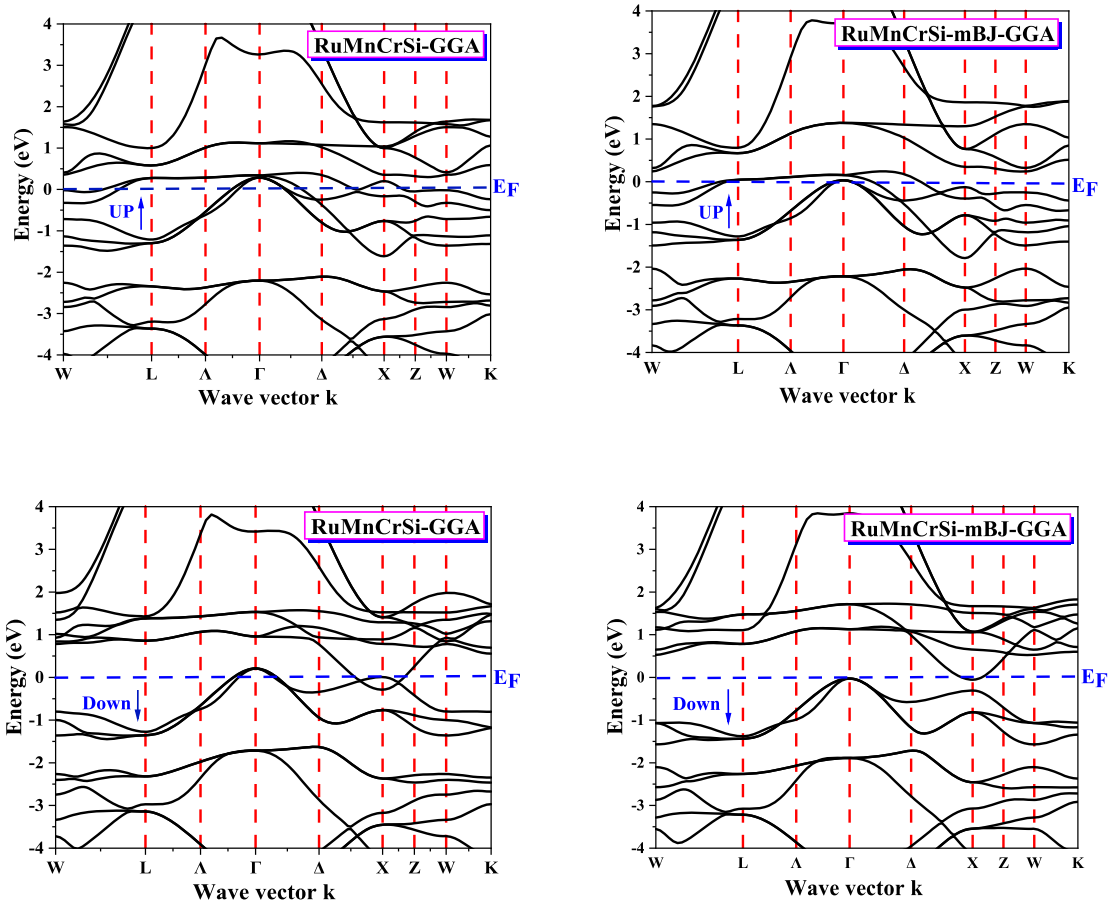

Figure 4. (Continued.)

Table 4. Energy gap values were determined using both the GGA and mBJ-GGA approximations.

Compounds	The spins	E_g(eV)	
		GGA	mBJ-GGA
NiMnCrAl-Type I	Up	0.070	/
	Down	0.221	0.585
RuMnCrSi-Type III	Up	/	/
	Down	/	0 [Gapless]

Furthermore, the main group element Z contributes one *s*-band and three degenerate *p*-bands, which are lower in energy compared to the *d*-bands. These *p*-bands play a critical role in enhancing the structural stability of the alloy by reducing the effective concentration of *d*-charge in the material. Particularly important are the non-bonding d-hybrids, which include the three occupied t_{1u} states and the two unoccupied e_u states. The spatial arrangement and energy alignment of these states are pivotal in determining the energy gap of the minority spin band, which directly influences the magnetic and electronic behaviors of the compound (see figure 6).

In compounds exhibiting a Type I crystal structure, the positioning of element X at site B and element Y at site D results in the formation of octahedral symmetry. This symmetry plays a crucial role in facilitating the initial hybridization between these elements. The hybridization process is further amplified through interactions with element X′ at site C, which gives rise to a complex network of hybrid states. The different hybridization patterns in Type I and Type III crystal structures, influenced by the atomic positions, lead to variations in the resulting band structures, affecting the electronic properties of the compounds. A notable observation in these materials is that the crystal structure remains stable even when the atomic positions of elements X and X′, or Y and Z, are interchanged. This stability is attributed to the inherent symmetry of space group 216, which ensures that such positional swaps do not alter the structural or electronic properties of the compound. This symmetry, therefore, reinforces the robustness of the material's characteristics under different

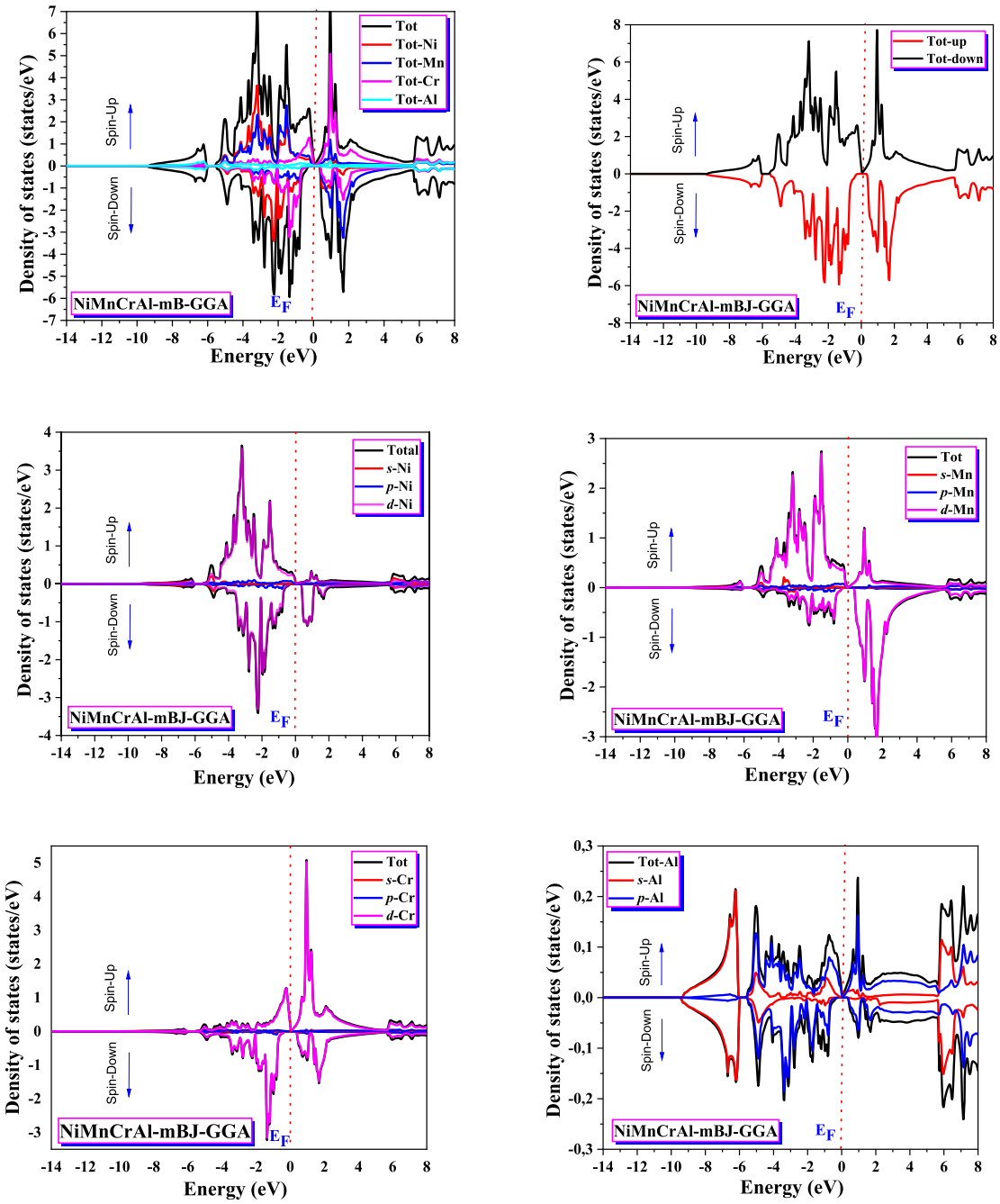

Figure 5. The total and partial state densities of NiMnCrAl in Type-I and RuMnCrSi in Type-III, calculated using the mBJ-GGA approximation.

atomic arrangements. For the Heusler compounds RuMnCrSi and NiMnCrAl, the total magnetic moments (M_{Tot}) at a pressure of 0 GPa are calculated to be 2 μ_B and 1 μ_B, respectively. These values are consistent with the predictions of the Slater-Pauling rule, which establishes a relationship between the magnetic moment and the number of valence electrons in the compound. This rule provides a convenient way to estimate the magnetic behavior of Heusler alloys, contributing to our understanding of their spintronic and magnetic properties. The relationship between the total number of valence electrons (N_v) and the number of spin-down states (N_d) in each unit cell is given by the equation $M_{Tot} = N_v - 2N_d$. For RuMnCrSi, N_v is 25, and for NiMnCrAl, Nv is 26. In both compounds, the number of spin-down states, N_d, is fixed at 12. These 12 spin-down states consist of one *s*-band, three *p*-bands, and eight *d*-bands, which are classified into the $2e_g$, $3t_{2g}$, and $3t_{1u}$ states. This model effectively explains the magnetic properties of the compounds and aligns with the experimentally observed values of the total magnetic moment.

At the Γ point in the Brillouin zone, the degeneracy of the bands is as follows: one for the s bands, three for the *p* bands, two for the *e* bands, and three for the *t* bands. These *e* and *t* bands arise from hybridization between

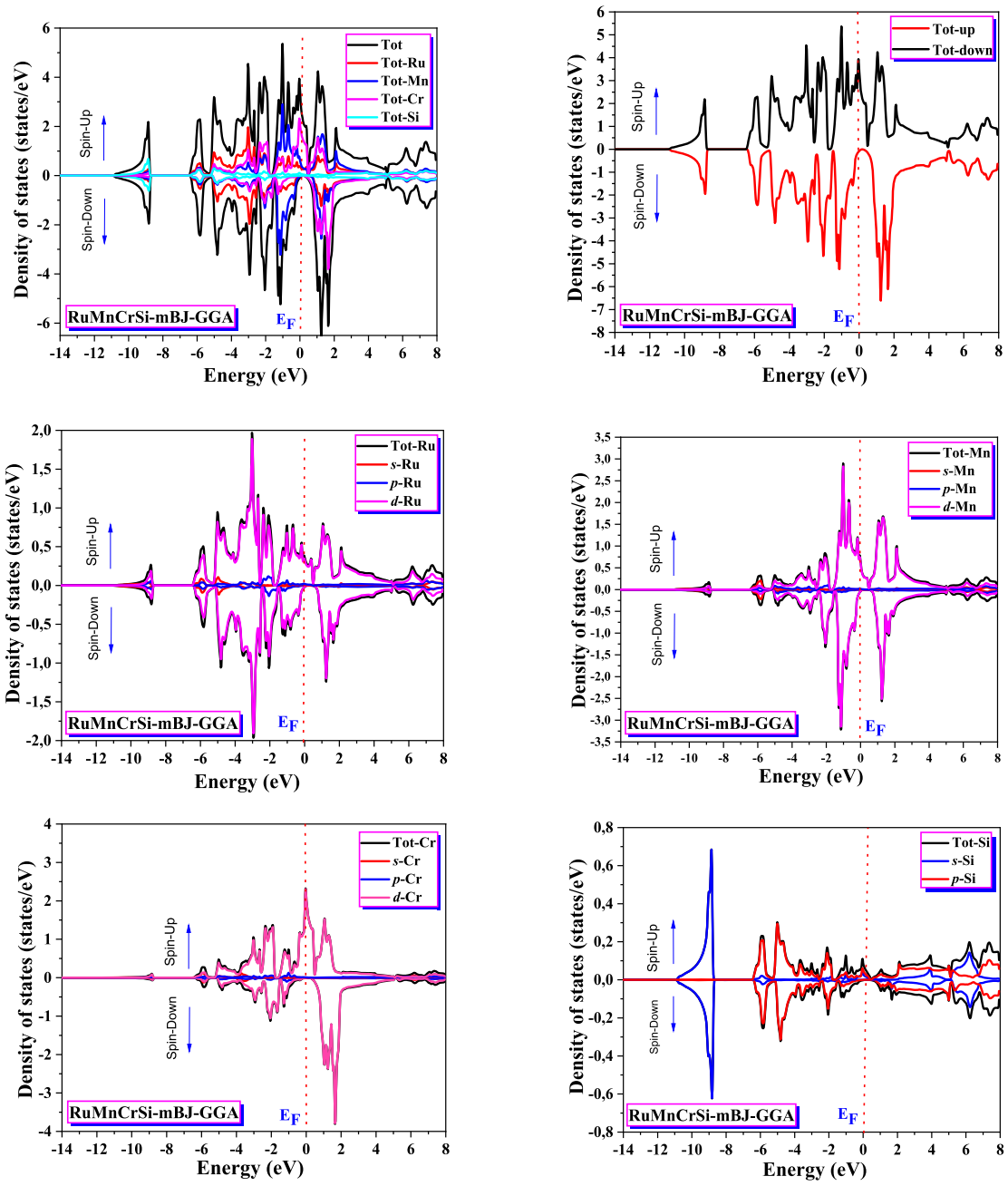

Figure 5. (Continued.)

the *3 d* orbitals of Ni, Mn, and Cr in NiMnCrAl, and between the *3 d* and *4 d* orbitals of Mn, Cr, and Ru in RuMnCrSi. This hybridization significantly influences the electronic properties of the compounds, contributing to their unique magnetic behavior.

The band structures of the quaternary Heusler alloys RuMnCrSi and NiMnCrAl reveal fully populated valence bands, which are formed by a combination of *s*, *p*, $2e_g$, $3t_{2g}$, $2e_u$, $3t_{1u}$, and $2e_g$ orbitals. These bands provide a comprehensive view of the electron distribution within the materials, reflecting the hybridization of atomic orbitals. The Fermi level, which is positioned at 0 eV, intersects the partially filled $3t_{2g}$ conduction band, indicating that both compounds exhibit metallic behavior in the spin-up channel. This suggests that the majority spin states are metallic, with conduction facilitated by the partially occupied $3t_{2g}$ states, as illustrated in figure 7. The conductive nature in the spin-up channel is consistent with the presence of these delocalized states, which allow for free electron movement. On the other hand, the spin-down band structure for both compounds shows completely filled valence bands, including the *s*, *p*, $2e_g$, $3t_{2g}$, and 3_{t1u} states. The Fermi level is positioned between the fully occupied 3t1u valence bands and the unfilled $2e_u$ conduction states. This placement results in a band gap in the spin-down channel, suggesting semiconductor behavior in this spin configuration. The absence

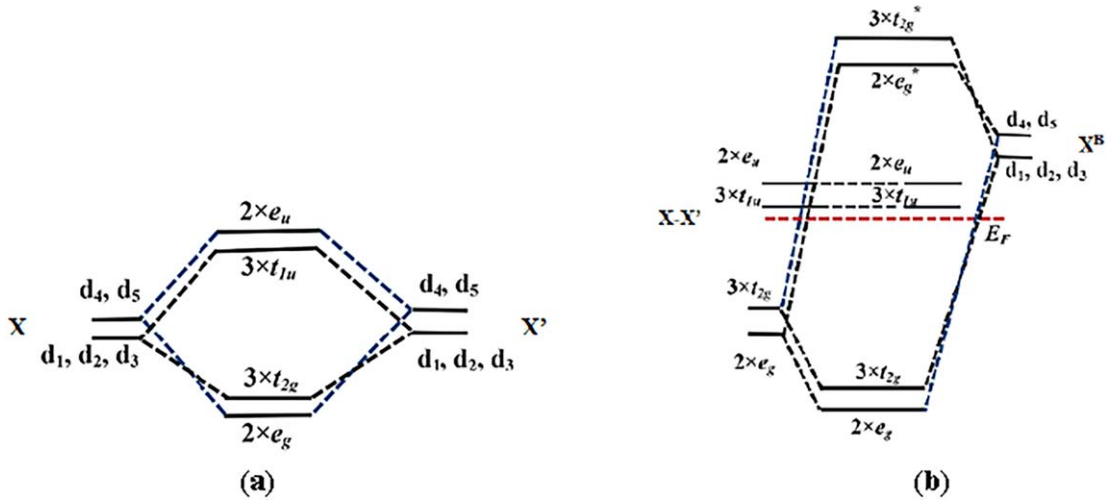

Figure 6. Potential hybridization schemes for spin-down bands in Type III structures: (a) Hybridization between atoms X and X′ at coordinates A and C, and (b) hybridization for compounds with $M_{Tot} = N_v - 24$.

of available states for conduction at the Fermi level in the spin-down channel leads to insulating or semiconducting characteristics for this spin state, as seen in figure 7.

To further confirm the presence of an energy gap in the spin-down channel, we performed detailed calculations of the total density of states (DOS) at the Fermi level, with an emphasis on spin polarization. The spin-polarized DOS provides valuable insights into the electronic structure, helping to identify whether the materials exhibit metallic, semiconducting, or insulating behavior. This analysis is crucial for understanding the electronic properties of these alloys and their potential applications in spintronic devices, where control over spin polarization and the presence of spin-dependent conduction channels is essential.

The equation used to calculate the total DOS at the Fermi level for a spin-polarized system is given by:

$$P = \frac{N(E_F)^{\uparrow} - N(E_F)^{\downarrow}}{N(E_F)^{\uparrow} + N(E_F)^{\downarrow}} \tag{6}$$

The Heusler quaternary alloys RuMnCrSi and NiMnCrAl are gaining significant attention in spintronics due to their exceptional electronic spin polarization properties, which play a crucial role in the advancement of spintronic technologies. These materials exhibit strong spin-polarized behaviors, making them promising candidates for applications such as spin filters, magnetic tunnel junctions, and other spintronic devices. To evaluate these spin polarization characteristics, the electronic spin polarization at the Fermi level was calculated using a standard method described by equation (5). This approach is widely recognized for its effectiveness in quantifying spin polarization in a variety of materials.

In this study, the spin polarization of both RuMnCrSi and NiMnCrAl was determined to be 100%, based on calculations performed with the mBJ-GGA approximation. This result, detailed in table 5, suggests that both compounds exhibit perfect spin polarization at the Fermi energy, indicating that they may serve as ideal spin-polarized materials for applications in the spintronic industry. The high degree of spin polarization is indicative of the compounds' potential for use in devices requiring full spin-polarization, such as spin valves or magnetic semiconductors, where the control of electron spin is crucial.

Further analysis of the density of states (DOS) confirms that the Heusler quaternary compounds, RuMnCrSi (Type III) and NiMnCrAl (Type I), exhibit ferrimagnetic semi-metallic properties using mBJ-GGA. This observation demonstrate that these compounds exhibit ideal spin-polarized behavior, which is a critical feature for spintronic applications. Therefore, these compounds hold significant promise as materials for future spintronic technologies, potentially contributing to the development of more efficient magnetic devices, such as spin transistors, magnetic memory devices, and spin-based logic systems [57].

Table 6 presents the computed local and total magnetic moments for the Heusler quaternary alloys RuMnCrSi and NiMnCrAl, using both the GGA and mBJ-GGA approximations. These calculations reveal that both alloys exhibit ferrimagnetic behavior, with the total magnetic moment measured at 2 μ_B for NiMnCrAl and 1 μ_B for RuMnCrSi. The magnetic properties of these compounds are predominantly governed by the localized magnetic moments of specific transition metal elements, particularly chromium (Cr) in NiMnCrAl and manganese (Mn) in RuMnCrSi. These elements contribute substantially to the net magnetic moment of the compounds. On the other hand, elements such as silicon (Si) in RuMnCrSi and aluminum (Al) in NiMnCrAl

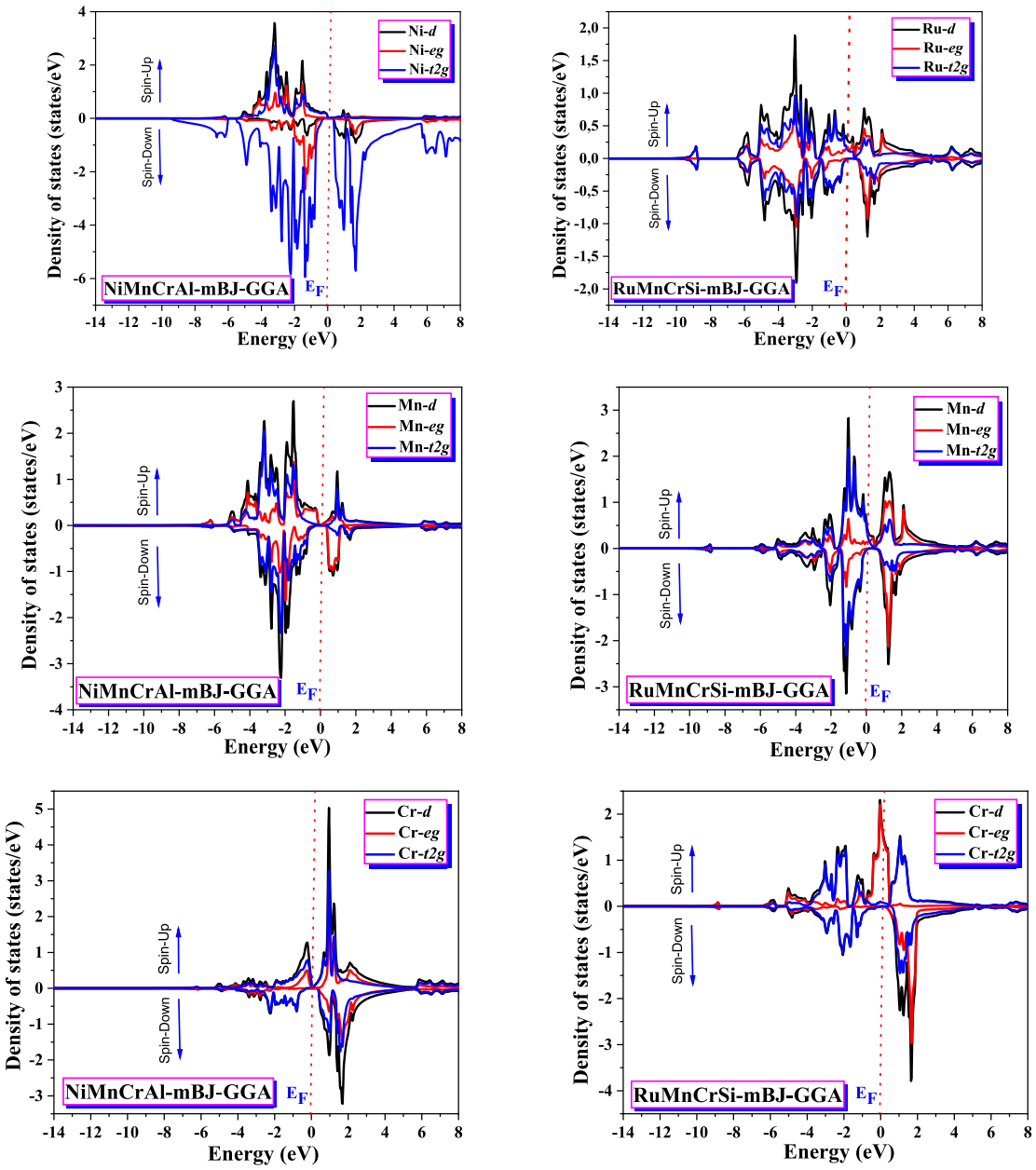

Figure 7. Partial state densities of the hybrid orbitals for majority and minority spins in NiMnCrAl and RuMnCrSi compounds, calculated using the mBJ-GGA approximation.

Table 5. The total electron density N(EF) for spin-up and spin-down states at the Fermi level, with *P* polarization, were evaluated using the GGA and mBJ-GGA methods.

	GGA			mBJ-GGA		
	$N(E_F)$		P	$N(E_F)$		P
	$N(E_F)\downarrow$	$N(E_F)\uparrow$		$N(E_F)\downarrow$	$N(E_F)\uparrow$	
NiMnCrAl	/	/	/	0.01	0.54	96%
RuMnCrSi	0.01	0.54	96%	0	0.44	100%

have a negligible effect on the overall magnetic moment, suggesting that their contribution to the material's magnetic properties is minimal. This observation highlights the dominant role of transition metals in dictating the magnetic characteristics of Heusler alloys. The results underscore the importance of the transition metal

Table 6. The total and partial magnetic moments (μ_β) were computed using the GGA and mBJ-GGA approximations.

Compounds	Parameters (μ_β/atom)	Our calculations		Theoretical calculations [36]
		GGA	mBJ-GGA	
NiMnCrAl	M(Interstitielle)	−0.03615	−0.12229	/
	M(Ni)	0.59624	0.65653	0.64
	M(Mn)	2.67439	2.94450	2.90
	M(Cr)	−1.21320	−1.45391	−1.49
	M(Al)	−0.02103	−0.02475	−0.02
	M(Tot)	2.00025	2.00008	2.00
RuMnCrSi	M(Interstitielle)	0.04277	0.05396	/
	M(Ru)	−0.02436	−0.01565	−0.03
	M(Mn)	−0.32599	−0.26134	−0.53
	M(Cr)	1.27376	1.19756	1.46
	M(Si)	−0.00418	0.00358	0.02
	M(Tot)	1.01072	1.00942	1.01

composition in determining the magnetic behavior of these compounds, which is a crucial factor in their potential use in magnetic devices, including sensors and actuators.

This observation highlights the critical role of transition metals, particularly Cr and Mn, in governing the magnetic behavior of Heusler alloys, with Si and Al atoms acting more as structural stabilizers without significantly altering the magnetic characteristics of the material.

2.3. Optical features

The study of optical properties in materials has become an invaluable approach for gaining a deeper understanding of their electronic characteristics. This analysis involves calculating key numerical parameters, such as the complex dielectric function, which plays a crucial role in describing how materials interact with electromagnetic waves. The complex dielectric function provides insight into the material's response to an external electromagnetic field, detailing both its absorptive and refractive behaviors. This function is essential for understanding phenomena like light absorption, refraction, and transmission, which are influenced by the material's electronic structure.

Furthermore, the dielectric function allows for the investigation of interband transitions, electron scattering, and plasmonic behaviors, offering a comprehensive picture of how a material might behave in optoelectronic applications, such as in solar cells, light-emitting devices, or sensors. By analyzing these characteristics, researchers can correlate the optical properties with the material's electronic structure and predict its potential applications in various fields. This approach not only helps to reveal fundamental material properties but also guides the design of new materials with tailored optical and electronic behaviors.

The complex dielectric function, typically represented as [58]:

$$\varepsilon(\omega) = \varepsilon_1(\omega) + i\varepsilon_2(\omega) \tag{7}$$

The imaginary part of the dielectric function, denoted as $\varepsilon_2(\omega)$, plays a crucial role in characterizing how a material absorbs light, as it directly correlates with the material's ability to interact with electromagnetic radiation. On the other hand, the real component, $\varepsilon_1(\omega)$, is primarily associated with the polarization response of the material to an external electric field. These components together provide a comprehensive understanding of a material's optical properties, influencing phenomena such as absorption, reflection, and refraction.

In this study, the imaginary part of the dielectric function, $\varepsilon_2(\omega)$, was computed using the mBJ-GGA approximation, which is known for its improved treatment of electronic correlations in materials. The calculations were performed over a broad energy range from 0 to 55 eV, as shown in figure 8(a), to capture both the low-energy and high-energy behavior of the material. The range of energy investigated ensures that the electronic transitions occurring within the material are well represented, from the low-energy excitations to the interband transitions in the ultraviolet and beyond. This range includes important electronic transitions between filled and unfilled states, which are responsible for the values of the imaginary dielectric component. The origin of each peak in the optical spectra can be traced to transitions between the upper valence bands and the lower conduction bands.

The two compounds, RuMnCrSi and NiMnCrAl, exhibit nearly identical spectra in the imaginary part of the dielectric function, indicating similar optical characteristics (see figure 8(a)). A key point to note in these optical

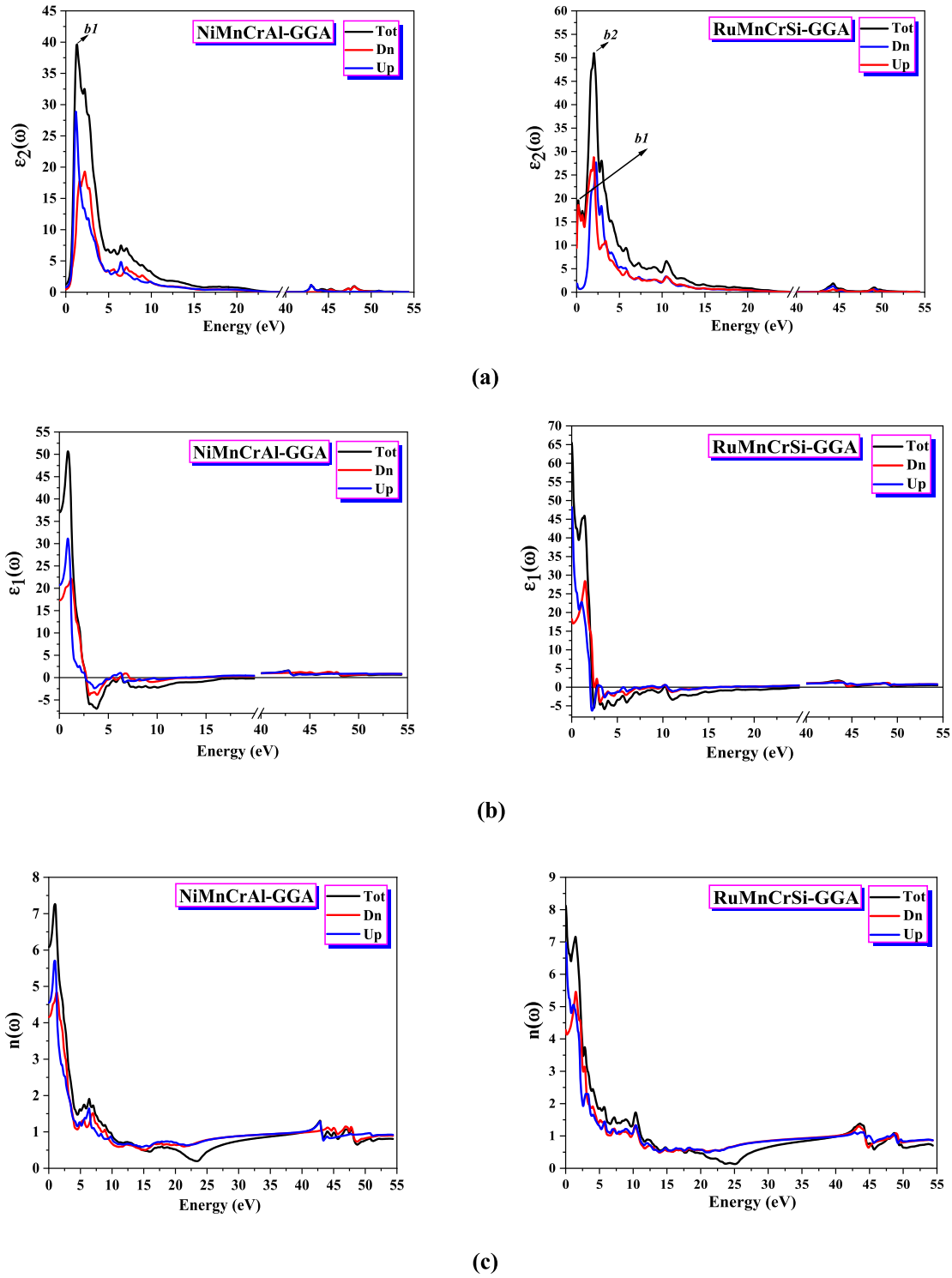

Figure 8. Variation of (a) real and (b) imaginary parts of the dielectric function, (c) refractive index, (d) extinction coefficient, (e) reflectivity, (f) absorption coefficient, (g) optical conductivity, and (h) energy loss function with photon energy for the RuMnCrSi and NiMnCrAl compounds, calculated using the mBJ-GGA approximation.

spectra is the absorption edge, which defines the boundary between the valence and conduction bands. This edge is a critical parameter, as it sets the energy threshold for the optical transitions, distinguishing between direct and indirect transitions from the valence to conduction bands.

The bands are identified based on their relative positions to the highest valence and the lowest conduction band, and the primary absorption level corresponds to the first transition from the upper valence band to the lower conduction band. Understanding this threshold is essential for evaluating the material's optical behavior and its potential use in applications such as optoelectronics, where light absorption is crucial.

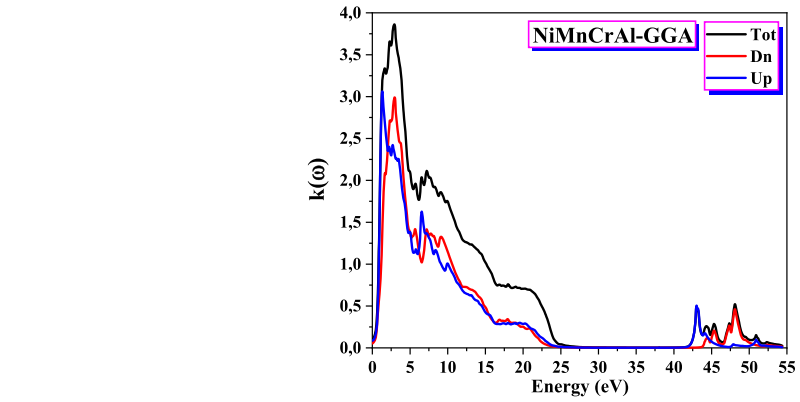

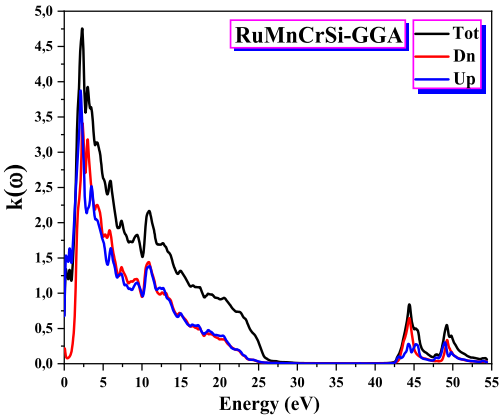

(d)

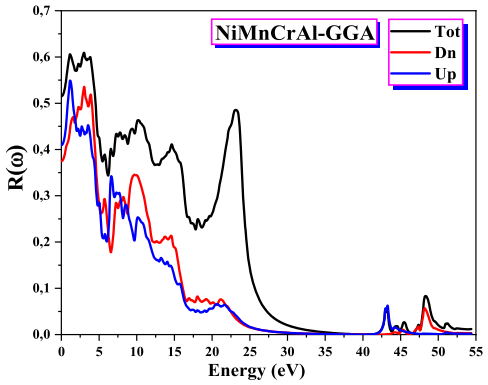

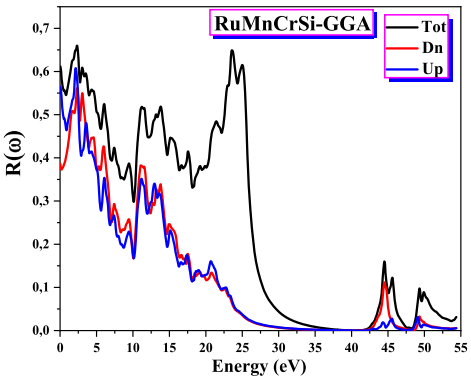

(e)

Figure 8. (Continued.)

For the first compound, NiMnCrAl, a primary peak b1 appears at an energy of 1.26355 eV. In contrast, for the second compound, RuMnCrSi, the fundamental peak, b2, is located at 2.02725 eV, accompanied by additional secondary peaks. The first secondary peak, b1, is observed at 0.17687 eV. In the infrared and visible regions, the peaks b1 and b2 are present. These peaks correspond to electronic transitions in the majority spin states for b1 and transitions in the minority spin states for b2. However, for RuMnCrSi, a mixture of majority and minority spin contributions is seen.

The dielectric functions of both RuMnCrSi and NiMnCrAl show absorption maxima in the minority spin states at 2.00004 eV and 2.19052 eV, respectively, and at 1.15648 eV and 2.05443 eV in the majority spin states. The optical absorption follows a certain order between the two compounds, $\varepsilon_2(RuMnCrSi) \rangle \varepsilon_2(NiMnCrAl)$, with the energy increasing as RuMnCrSi transitions into NiMnCrAl. This shift can be attributed to the decrease in the band gap as we move from NiMnCrAl to RuMnCrSi.

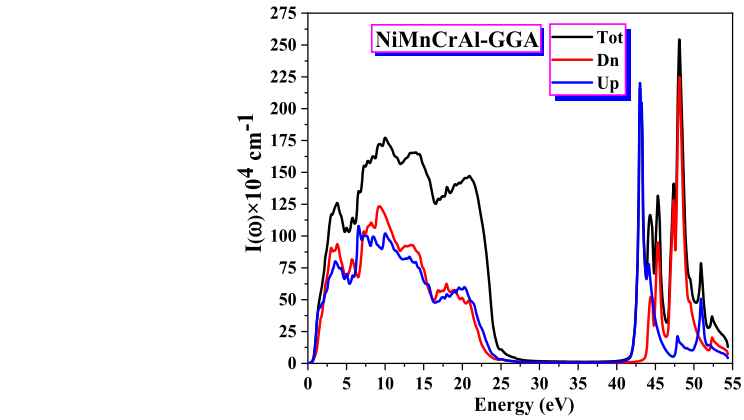

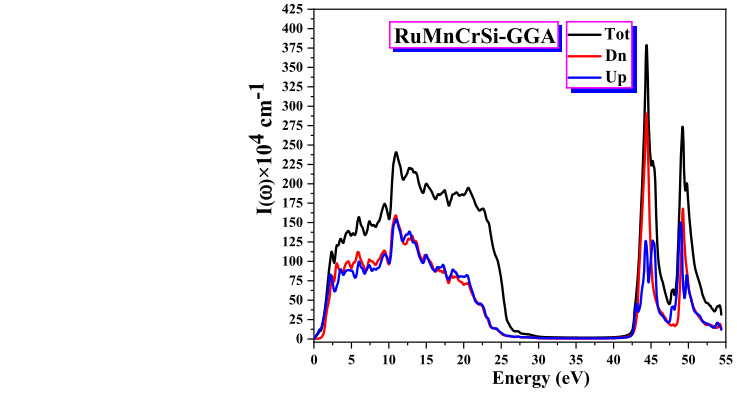

(f)

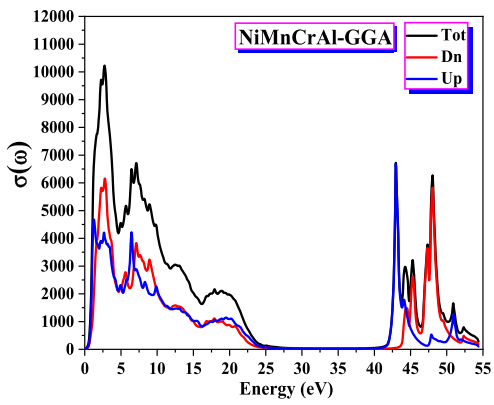

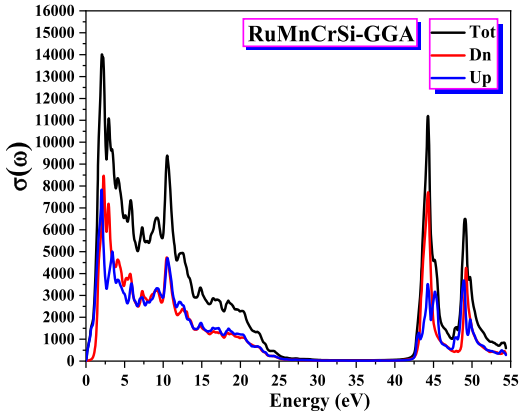

(g)

Figure 8. (Continued.)

The real part of the dielectric function is obtained from the imaginary part using the Kramers-Kronig transformations [59], as shown in figure 8(b). The static dielectric constants, calculated from the zero-frequency limits $\varepsilon_1(0)$, are presented in table 7. The optical spectra of both compounds are similar, though there are some differences, particularly in the peak positions and intensities. As the photon energy increases, the real part of the dielectric function exhibits a positive correlation, initially rising and reaching significant peaks before eventually dropping to zero. Following a minimum, the dispersive component of the dielectric function steadily approaches zero. According to the mBJ-GGA calculations, significant peaks in the dielectric function are observed at energies of 0.85716 eV for NiMnCrAl and 0.01361 eV for RuMnCrSi. These values correspond to distinct optical transitions that lie within the infrared region of the electromagnetic spectrum. The positioning of these peaks indicates that both materials exhibit strong optical responses at infrared wavelengths, which is crucial for understanding their potential applications in infrared optics and optoelectronics. The real part of the

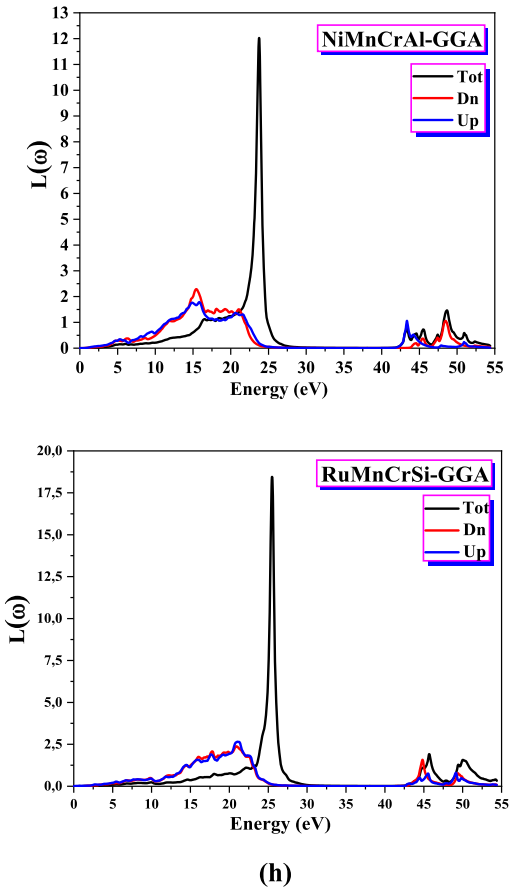

Figure 8. (Continued.)

Table 7. The $\varepsilon_1(0)$ and $n(0)$ values were obtained using the GGA and mBJ-GGA methods.

Compounds	$\varepsilon_1(0)$			n(0)		
	Spins	GGA	mBJ-GGA	Spins	GGA	mBJ-GGA
NiMnCrAl	Up	19.6436	20.7398	Up	4.43256	4.55493
	Down	23.5538	17.2740	Down	4.85436	4.15654
	Total	42.1974	37.0138	Total	6.49709	6.08474
RuMnCrSi	Up	60.7105	48.2331	Up	7.85102	6.97787
	Down	19.4217	18.2495	Down	4.40860	4.27666
	Total	79.1322	65.4826	Total	8.94147	8.12124

dielectric function reaches zero at 2.6853 eV and 2.2624 eV for NiMnCrAl and RuMnCrSi, respectively, and continues to decrease gradually to zero again at approximately 23.7614 eV and 25.5090 eV for NiMnCrAl and RuMnCrSi, respectively. RuMnCrSi exhibits the highest intensity peak within this range, suggesting stronger polarization or a more significant electronic transition at this energy. On the other hand, NiMnCrAl presents a slightly less intense peak, indicating that its electronic response is weaker in comparison to RuMnCrSi. The differences in peak intensity may be attributed to the variations in electronic structure and band interactions of the materials.

A smaller energy gap (E_g) is positively correlated with a higher static dielectric constant ($\varepsilon_1(0)$), consistent with Penn's model $\varepsilon_1(0) \approx 1 + \left(\frac{\hbar\omega_p}{E_g}\right)^2$ [60], where $\hbar\omega_P$ represents the plasma energy. The RuMnCrSi compound exhibits significant anisotropy in the real part of its dielectric function, a feature not observed in the NiMnCrAl compound.

The refractive index determines the degree of light reflection at the material interface, and in optical devices, it plays a crucial role in setting the critical angle for total internal reflection. The optical properties of these

compounds are significant for various applications. The refractive index spectra, shown in figure 8(c), closely follow the pattern of the real part of the dielectric function. Excitonic transitions can be identified in the refractive index spectra, where distinct peaks appear at the energy gap edge. For NiMnCrAl and RuMnCrSi, the refractive indices at zero frequency are n(0) = 6.08474 and n(0) = 8.12124, respectively, with RuMnCrSi showing the highest refractive index. The refractive index increases with frequency up to 1 eV, after which it decreases up to 23 eV, exhibiting nonlinear characteristics. The static refractive indices n(0) are listed in the table alongside other relevant data. To our knowledge, there are no available empirical or theoretical values for comparison.

Figure 8(d) illustrates the variation of the extinction coefficient as a function of photon energy for the compounds studied. The spectra show slight differences in certain regions. The extinction coefficient reaches its peak value at photon energies of 2.9281 eV (2.2876 eV) for NiMnCrAl (RuMnCrSi), falling within the visible spectrum. This peak corresponds to interband transitions between minority and majority states. After this peak, the extinction coefficient decreases rapidly as the photon energy continues to rise for both compounds.

As shown in figure 8(e), the reflectivity for the minority spin channel begins at 37.47% and 38.64%, while for the majority spin states, it starts at 40.96% and 56.45%. This results in total reflectivity values of 51.51% for NiMnCrAl and 61.17% for RuMnCrSi. The primary peak in reflectivity occurs at energies of 3.0078 eV for NiMnCrAl and 2.3557 eV for RuMnCrSi. Notably, RuMnCrSi exhibits higher reflectivity compared to NiMnCrAl.

Both materials demonstrate high absorption coefficients (10^4 cm^{-1}), with three prominent peaks, labeled b1, b2, and b3, observed for each compound (see figure 8(f)). At lower energy values, the absorption coefficient rises rapidly, reaching the first peak (b1) in the near-ultraviolet region. This is followed by a decrease, an increase to the second peak (b2), and another drop before reaching the third peak (b3). Peaks b2 and b3 are clearly in the far-ultraviolet range. The observed peak values for NiMnCrAl are 10.9525 eV, 44.3953 eV, and 49.2118 eV, while for RuMnCrSi, they occur at 10.9798 eV, 44.4226 eV, and 49.2118 eV. These peaks arise from interband and intraband transitions within the electronic band structure, involving different symmetry points. The compounds are shown to effectively absorb energy across the low to mid-ultraviolet spectrum. The absorption spectra display maxima in energy ranges of 2.3265–23.0344 eV, 42.7627–43.4974 eV, and 47.0893–48.9124 eV for NiMnCrAl, and 2.1633–24.2861 eV, 43.9328–45.6471 eV, and 48.8308–49.9465 eV for RuMnCrSi. RuMnCrSi exhibits the highest absorption coefficient, followed by NiMnCrAl. Due to their broad absorption bands and high absorption intensities, these Heusler quaternary materials have potential for applications in optoelectronic devices.

Optical conductivity $\sigma(\omega)$ measures a material's ability to transmit light. The relationship between the oscillating electric field $E(\omega)$ and the current density $j(\omega)$ is described by the equation, $j(\omega) = E(\omega)\sigma(\omega)$, as outlined in reference [61]. At specific frequencies $\omega \rightarrow 0$, optical conductivity transforms into electrical conductivity, and it is directly linked to the imaginary part of the dielectric function [62]. Figure 8(g) presents the optical conductivity spectrum, which exhibits multiple peaks corresponding to electronic transitions. Distinct boundaries appear in the energy ranges of 1.0204–10.4899 eV and 42.5178–49.1301 eV for NiMnCrAl, and 1.2925–12.7757 eV and 43.2253–50.2730 eV for RuMnCrSi, all falling within the ultraviolet region.

The electron energy loss plays a key role in characterizing the energy lost by high-velocity electrons as they travel through a solid. The peaks present in the L(ω) spectrum are indicative of plasmon excitations. Figure 8(h) shows that the highest energy peak is observed at 24.8499 eV. The compounds NiMnCrAl and RuMnCrSi exhibit significant peaks at 23.7614 eV and 25.5090 eV, respectively. The energy loss spectra for NiMnCrAl and RuMnCrSi show notable values within the energy ranges of 22.4358–24.4494 eV and 24.1229–26.2998 eV, respectively. The average energy value at the peak of the energy loss function corresponds to the plasma frequency ωp. Specifically, the peak plasma energies $\hbar\omega$p for NiMnCrAl and RuMnCrSi are 23.7614 eV and 25.5090 eV, respectively. The plasma frequencies for these materials are 4.0122×10^{16} s^{-1} for NiMnCrAl and 3.9502×10^{16} s^{-1} for RuMnCrSi.

2.4. Thermoelectric parameters

The increasing global energy demand has driven researchers to explore new materials and technologies that can effectively transform thermal energy into electrical power. Thermoelectric (TE) materials show great potential for these applications. These materials exploit the Seebeck or Peltier effects, which are essential for generating electrical energy. Consequently, TE materials have a wide range of potential uses in energy systems [63, 64]. An ideal thermoelectric material typically possesses the following features: low electronic conductivity (σ), high Seebeck coefficient (S), and low thermal conductivity (k). In contrast, the thermoelectric performance is quantified by the figure of merit (ZT) and the power factor (PF) = $S^2\sigma$. The goal of this study is to evaluate several thermoelectric properties of RuMnCrSi and NiMnCrAl, including carrier concentration (n), electrical conductivity (σ), electronic thermal conductivity (k_e), Seebeck coefficient (S), and figure of merit (ZT). These

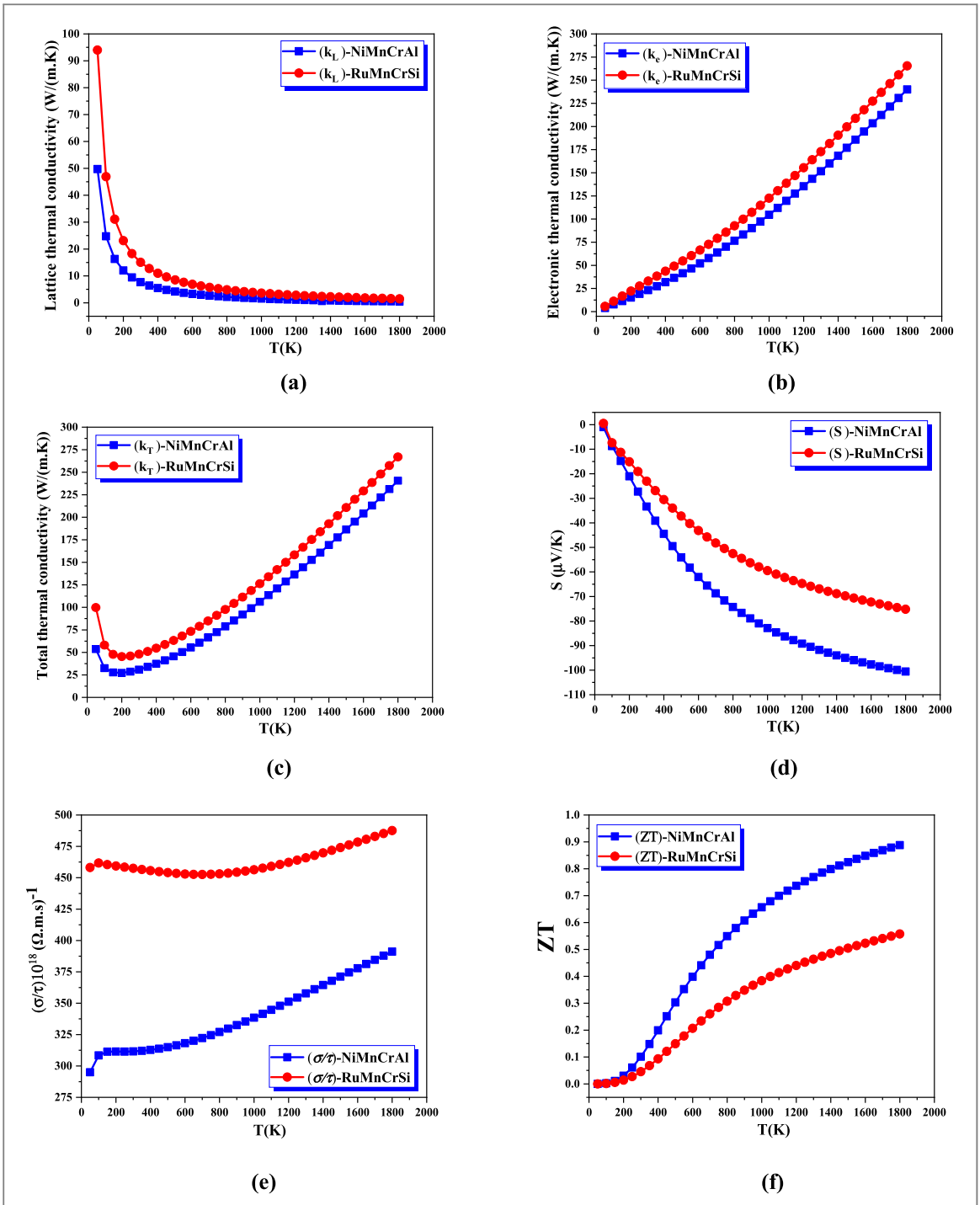

Figure 9. Temperature variation of (a) lattice thermal conductivity (k_L), (b) electronic thermal conductivity (k_e), (c) total thermal conductivity (k_T), (d) Seebeck coefficient (S), (e) electrical conductivity as a function of relaxation time, and (f) figure of merit (ZT) for NiMnCrAl and RuMnCrSi compounds, estimated using the mBJ-GGA approach.

properties are analyzed using the semiclassical Boltzmann transport approach via the BoltzTrap code [31]. Furthermore, the lattice thermal conductivity (k_L) is calculated based on Slack's empirical formula [65]. Figure 9 illustrates the variations of these parameters with temperature. To ensure accurate results, a constant relaxation time of 10^{-14} s was assumed.

Figures 7(a)–(b) present the thermal conductivity components, including the lattice thermal conductivity (k_L) and the electronic thermal conductivity (k_e), which together contribute to the total thermal conductivity (k_T). The lattice thermal conductivity (k_L) for the compounds RuMnCrSi and NiMnCrAl was calculated using Slack's model [66, 67] over a temperature range from 50 K to 1800 K, as shown in figure 7(a). At temperatures of 300 K and 1000 K, the thermal conductivity values (k_L) for RuMnCrSi and NiMnCrAl are 15.0478 (7.6945) W mK^{-1} and 3.6207 (1.5531) W mK^{-1}, respectively. The Grüneisen parameter (γ) and Debye temperature (θ_D) for RuMnCrSi (NiMnCrAl) were found to be 606.83 K (534.72 K) and 2.7873 (2.1216), respectively, based on the quasi-harmonic

Debye approximation technique [68] at 300 K. As seen in figure 7(a), the lattice thermal conductivity (k_L) decreases with increasing temperature for both compounds.

The electronic thermal conductivity (k_e) values for the RuMnCrSi and NiMnCrAl compounds were calculated and are presented in figure 9(b). The data shows a clear positive correlation between ke and temperature, with the value of (k_e) increasing substantially as the temperature rises. Specifically, for RuMnCrSi (NiMnCrAl), k_e increases from 32.9767 (23.1947) W mK^{-1} at 300 K to 122.5902 (104.6052) W mK^{-1} at 1000 K. Figure 9(c) illustrates that the total thermal conductivity (k_T) decreases with increasing temperature, reaching a minimum around 200 K for both compounds. This suggests a reduction in phonon–phonon interaction at lower temperatures. As the temperature increases, phonon interactions become more prominent, leading to a decline in k_T. At 200 K, the thermal conductivity values are approximately 45.3052 W mK^{-1} for RuMnCrSi and 27.2535 W mK^{-1} for NiMnCrAl, confirming the reliability of these measurements.

The Seebeck coefficient (S) is a key parameter that offers important information about a material's thermoelectric properties. Figure 9(d) displays the temperature-dependent Seebeck coefficient (S) for the compounds under investigation. The calculated values of S for the CoIrMnSn compound show negative values across all temperatures, which indicates n-type conductivity. This behavior suggests that electrons are the dominant charge carriers, contributing significantly to electrical conduction. In contrast, for the RuMnCrSi and NiMnCrAl compounds, the Seebeck coefficient decreases as temperature increases, shifting from $-23.0339\,\mu V\,K^{-1}$ and $-33.3523\,\mu V\,K^{-1}$ at 300 K to $-59.4690\,\mu V\,K^{-1}$ and $-82.8731\,\mu V\,K^{-1}$ at 1000 K, respectively. Energy band theory suggests that conduction in conductors is facilitated by the abundant availability of free charges, while in semiconductors, charge generation requires external energy input. This behavior has been observed in various studies, where thermoelectric materials with metallic-like conductivity exhibit a decline in S at high temperatures due to increased carrier excitation and bipolar effects [68, 69]. The metallicity in thermoelectric compounds does not necessarily imply poor performance but rather indicates that optimizing carrier concentration is essential for enhancing ZT.

Figure 9(e) shows the (σ/τ) values for the studied compounds over a temperature range from 50 K to 1400 K. The graph reveals a clear temperature dependence of the (σ/τ) ratio. For RuMnCrSi (NiMnCrAl), the (σ/τ) values rise from 457.5092×10^{18} (311.6191×10^{18}) $(\Omega\,m\,s)^{-1}$ at 300 K to 456.4071×10^{18} (338.4608×10^{18}) $(\Omega\,m\,s)^{-1}$ at 1000 K, underscoring the materials' excellent ability to convert thermal energy to electrical power. Ideal thermoelectric materials are characterized by low thermal conductivity (k_T) and high electrical conductivity (σ), both of which are observed in the compounds studied here, indicating their potential for high thermoelectric performance.

Figure 9(f) presents the ZT graphs from the computational analysis of our materials. The RuMnCrSi and NiMnCrAl half-Heusler alloys show significant peak ZT values of 0.5576 and 0.8880, respectively, at 1800 K, demonstrating their potential for thermoelectric applications. Notably, the performance of these materials improves with increasing temperature, making them more suitable for thermoelectric energy conversion.

Recent studies on quaternary Heusler alloys have demonstrated promising half-metallic and thermoelectric properties, making them suitable for spintronic and energy applications. Xiong *et al* [70] investigated CoFeTiZ and CoFeVZ (Z = Al, Ga, Si, Ge, As, Sb), revealing large half-metallic gaps that enhance spin polarization. While these materials exhibit excellent magnetic behavior, our studied RuMnCrSi and NiMnCrAl alloys show superior thermoelectric properties, making them versatile for both thermoelectric and spintronic applications.

Similarly, Khandy and Chai [71] explored FeRhCrZ (Z = Si, Ge) alloys, reporting high thermoelectric efficiency with mechanical and phonon stability. However, our results indicate improved thermal conductivity reduction mechanisms, leading to enhanced ZT values. Moreover, Liu *et al* [72] studied CrLaCoZ compounds and found a high Seebeck coefficient, but our materials demonstrate a better balance between electrical conductivity and lattice thermal conductivity, which is crucial for optimizing thermoelectric performance.

In contrast, Ishfaq *et al* [73] examined Sr_2LaTaO_6 and Sr_2LuTaO_6 double perovskites, highlighting their optoelectronic and thermoelectric efficiency with a figure of merit ($zTe \approx 0.8$) at room temperature. While their focus was on perovskite structures, our Heusler alloys exhibit half-metallicity alongside high thermoelectric performance, providing additional advantages for spintronic applications. These comparisons underscore the novelty of our study, as our materials offer a unique combination of thermoelectric, electronic, and magnetic properties that set them apart from previously reported quaternary Heusler alloys.

Figure 10(a) shows how the (σ/τ) ratio varies with charge carrier concentration for the NiMnCrAl and RuMnCrSi compounds. As hole concentration rises, the (σ/τ) ratio declines. This observation is consistent with the temperature-independent nature of the (σ/τ) function, which is governed by the density of states (DOS) and charge transport mechanisms within the material, rather than by temperature. The higher level of delocalization in the valence band, compared to the conduction band, near the Fermi level in the NiMnCrAl (RuMnCrSi) compounds further explains this behavior. Additionally, the data show that p-type materials (like NiMnCrAl) exhibit a lower (σ/τ) ratio than n-type materials (like RuMnCrSi), reinforcing the connection between charge carrier concentration and material conductivity [74].

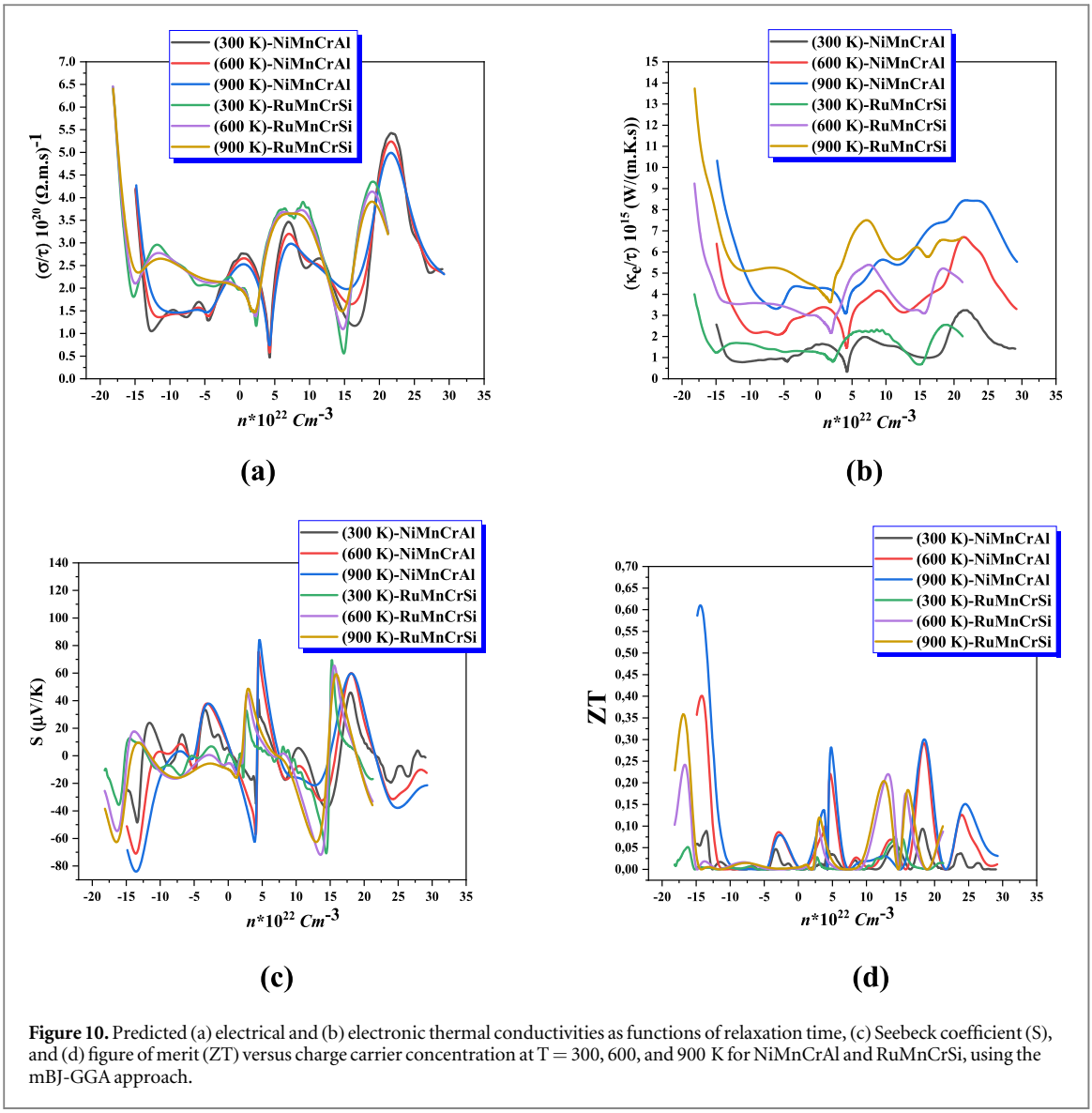

Figure 10. Predicted (a) electrical and (b) electronic thermal conductivities as functions of relaxation time, (c) Seebeck coefficient (S), and (d) figure of merit (ZT) versus charge carrier concentration at T = 300, 600, and 900 K for NiMnCrAl and RuMnCrSi, using the mBJ-GGA approach.

Figure 10(b) shows the relationship between the (k_e/τ) ratio and charge carrier concentration for the NiMnCrAl and RuMnCrSi alloys. The results indicate that as the charge carrier concentration increases through hole doping, the (k_e/τ) ratio decreases. In contrast, an increase in electron concentration leads to a higher (k_e/τ) value. While the value of electrical conductivity (σ) remains unaffected by temperature, the thermal conductivity (k_e) exhibits a clear temperature dependence. This can be explained by the positive correlation between k_e and temperature, indicating that thermal conductivity increases as temperature rises. In contrast, the behavior of electrical conductivity (σ) does not show this temperature dependence.

At high charge carrier concentrations, the Seebeck coefficients (S) of our materials are primarily influenced by temperature, showing a decreasing trend as temperature increases. This behavior is attributed to the narrow bandgaps of the compounds, which make the Seebeck coefficient more susceptible to the bipolar effect. The bipolar thermal effect, influenced by minority carrier mobility, becomes more pronounced at higher temperatures. Consequently, the maximum absolute values of S decrease and approach regions with higher carrier concentrations. Notably, n-type compounds show higher Seebeck coefficients than p-type ones, as seen in figure 10(c).

The impact of temperature and charge carrier concentration on the ZT curves as shown in figure 10(d). At elevated temperatures, the materials display behaviors commonly associated with thermoelectric half-Heusler compounds. N-type compounds exhibit notably higher ZT values than p-type ones. At 900 K, the p-type NiMnCrAl and RuMnCrSi compounds attain peak ZT values of 0.3004 and 0.1977, respectively, while the n-type counterparts demonstrate ZT values of 0.6101 and 0.3583. The corresponding carrier concentrations for these materials are 0.1849×10^{20} cm^3 and 0.1290×10^{20} cm^3 for *p*-type, and -0.1421×10^{20} cm^3 and -0.1688×10^{20} cm^3 for *n*-type. Moreover, figure 10(d) shows ZT as a function of carrier concentration,

reinforcing that optimizing doping levels is key to maintaining high thermoelectric performance. The peaks in ZT suggest that there exists an optimal carrier density for maximizing efficiency. Similar trends in thermoelectric performance improvement at high temperatures have been reported in recent literature [75], further supporting our findings.

The thermoelectric performance of various materials has been investigated, revealing a range of ZT values under different conditions. For *n*-type $Bi_2Al_4Se_8$, a ZT of 0.76 is achieved at a carrier concentration of $n = -6.448 \times 10^{18}$ cm^{-3} [76]. Similarly, $CuPN_2$ exhibits a ZT of 0.99 at $n = -1.7 \times 10^{19}$ cm^{-3} for n-type conduction, while HPN_2 reaches a comparable ZT for *p*-type conduction at $n = 1.4 \times 10^{19}$ cm^{-3}. Additionally, $LiPN_2$ and $NaPN_2$, when *p*-type, show thermoelectric performance at $n = 0.4 \times 10^{19}$ cm^{-3} [77, 78]. At 700 K, $CaZn_2Sb_2$ demonstrates a ZT of 0.33 [79]. For the *n*-type LiCrZ (Z = S, Se, Te) compounds, the ZT values are 0.68, 0.9495, and 0.9507, respectively [80]. In CoFeTiGe and CoFeCrGe, the ZT values for *n*-type conduction are 0.25 and 0.404, while for *p*-type conduction, they are 0.243 and 0.644**, respectively [81]. For materials with spin-polarized transport, RbCrS, RbCrSe, and RbCrTe exhibit maximum ZT values in the spin-down direction of 0.81355, 0.62249, and 1.02846, respectively [82]. Furthermore, at room temperature, the $ScNbNi_2Sn_2$ compound displays a relatively low lattice thermal conductivity ($\kappa_L = 5.30776$ W m·K^{-1}) and achieves a maximum ZT of 0.64 at 900 K [83]. RuMnCrSi, with its gapless nature, holds promise for both spintronic and thermoelectric applications. Its spin-polarized conduction enables use in magnetic tunnel junctions and spintronic memory. Unlike Ba_2XIO_6 (X = Ag, Na) perovskites [84], which have wide bandgaps (1.9–3.2 eV) and ZT values of 0.63–0.75, RuMnCrSi's high electrical conductivity enhances thermoelectric performance through carrier optimization. While its ZT (0.3583 at 900 K) is lower, its spin-polarized transport offers potential for integrated spintronic-thermoelectric devices, making it a strong candidate for energy and magnetic applications. Our ongoing work continues to investigate these materials' behavior at varying temperatures, reinforcing the reliability of the trends we have established in earlier research.

3. Conclusion

This study employed spin-polarized density functional theory (DFT) within the mBJ-GGA framework to investigate the electronic, magnetic, mechanical, optical, and thermoelectric properties of the quaternary Heusler compounds RuMnCrSi (Type III) and NiMnCrAl (Type I). Our results reveal that both compounds exhibit semi-metallic behavior, with RuMnCrSi possessing a minority-spin band gap of 0.806 eV, while NiMnCrAl remains gapless. This distinct spin-polarized electronic structure suggests potential applications in spintronic devices such as magnetic tunnel junctions and spin valves.

The calculated total magnetic moments are 2 μB for NiMnCrAl and 1 μB for RuMnCrSi, with significant contributions from Mn and Cr atoms, confirming their ferrimagnetic nature. This tunable magnetism enhances their suitability for magnetic sensors and memory devices. Optically, both materials exhibit strong ultraviolet (UV) absorption, indicating their potential in UV photodetectors and optoelectronic applications.

Thermoelectric calculations reveal promising performance at high temperatures, with maximum ZT values of 0.6101 for NiMnCrAl (p-type) and 0.3583 for RuMnCrSi (n-type) at 900 K, demonstrating their viability for thermoelectric power generation and cooling applications. The mechanical stability of these compounds, supported by their computed elastic constants, further reinforces their potential for industrial deployment.

Overall, the combination of semi-metallic electronic properties, ferrimagnetism, UV absorption, and thermoelectric performance positions RuMnCrSi and NiMnCrAl as strong candidates for next-generation spintronic, optoelectronic, and thermoelectric devices. Future experimental validation, along with further studies on doping effects and environmental stability, will be crucial for optimizing their practical applications.

Data availability statement

The data cannot be made publicly available upon publication because they are not available in a format that is sufficiently accessible or reusable by other researchers. The data that support the findings of this study are available upon reasonable request from the authors.

ORCID iDs

H Baaziz https://orcid.org/0000-0003-4860-2740
Z Charifi https://orcid.org/0000-0003-3875-4716

References

[1] de Groot R A, Mueller F M, Engen P G v and Buschow K H J 1983 *Phys. Rev. Lett.* **50** 2024
[2] Zutic I, Fabian J and Das Sarma S 2004 *Rev. Mod. Phys.* **76** 323
[3] Hirohata A and Takanashi K 2014 *J. Phys. D: Appl. Phys.* **47** 193001
[4] Felser C and Fecher G H (ed) 2013 *Spintronics: From Materials to Devices* 1st ed. (Springer)
[5] Galanakis I and Dederichs P H (ed) 2005 Half-metallic alloys: fundamentals and applications 1st ed*Lect. Notes Phys.* 676 (Springer)
[6] Kato H, Okuda T, Okimoto Y, Tomioka Y, Oikawa K, Kamiyama T and Tokura Y 2004 *Phys. Rev.* B **69** 184412
[7] Stroppa A, Picozzi S, Continenza A and Freeman A 2003 *Phys. Rev.* B **68** 155203
[8] Akai H 1998 *Phys. Rev. Lett.* **81** 3002
[9] Soulen R Jr *et al* 1998 *Science* **282** 85
[10] Galanakis I and Mavropoulos P 2003 *Phys. Rev.* B **67** 104417
[11] Galanakis I, Dederichs P H and Papanikolaou N 2002 *Phys. Rev.* B **66** 174429
[12] Skaftouros S, Ozdogan K, Sasıoglu E and Galanakis I 2013 *Phys. Rev.* B **87** 024420
[13] Ozdogan K, Sasıoglu E and Galanakis I 2013 *J. Appl. Phys.* **113** 193903
[14] Wurmehl S, Fecher G H, Kandpal H C, Ksenofontov V, Felser C, Lin H-J and Morais J 2005 *Phys. Rev.* B **72** 184434
[15] Felser C and Hirohata A (ed) 2005 Heusler alloys: properties, growth, applications 1st ed.*Springer Ser. Mater. Sci.* 222 (Springer International Publishing)
[16] Fong C-y, Pask J E and Yang L H 2013 *Half-Metallic Materials and Their Properties* 2 (World Scientific)
[17] Block T, Felser C, Jakob G, Ensling J, Mühling B, Gütlich P and Cava R 2003 *J. Solid State Chem.* **176** 646
[18] C *et al* 2003 *J. Phys. Condens. Matter* **15** 7019
[19] Galanakis I and Phys J 2004 *Condens. Matter* **16** 3089
[20] Dai X, Liu G, Fecher G H, Felser C, Li Y and Liu H 2009 *J. Appl. Phys.* **105** 07E901
[21] Alijani V *et al* 2011 *Phys. Rev.* B **84** 224416
[22] Alijani V, Winterlik J, Fecher G H, Naghavi S S and Felser C 2011 *Phys. Rev.* B **83** 184428
[23] Gao G, Hu L, Yao K, Luo B and Liu N 2013 *J. Alloys Cmpd.* **551** 539
[24] Gao Q, Opahle I and Zhang H 2019 *Phys. Rev. Mater.* **3** 024410
[25] Aull T, Sasıoglu E, Maznichenko I, Ostanin S, Ernst A, Mertig I and Galanakis I 2019 *Phys. Rev. Mater.* **3** 124415
[26] Blaha P, Schwarz K, Sorantin P and Trickey S B 1990 *Comput. Phys. Commun.* **59** 399–415
[27] Schwarz K, Blaha P and Madsen G K H 2002 *Comput. Phys. Commun.* **147** 71–6
[28] Blaha P, Schwarz K, Madsen G, Kvasnicka D and Luitz J *Materials Chemistry, TU Vienna* http://wien2k.at
[29] Monkhorst H J and Pack J D 1976 *Phys. Rev. B: Solid State* **13** 5188
[30] Jamal M, Bilal M, Ahmad I and Jalali-Asadabadi S 2018 *J. Alloys Compd.* **735** 569–79
[31] Golesorkhtabar R, Pavone P, Spitaler J, Puschnig P and Draxl C 2013 *Comput. Phys. Commun.* **184** 1861
[32] Madsen G K H and Singh D J 2006 *Comput. Phys. Commun.* **175** 67–71
[33] Otero-de-la-Roza A and Luaña V 2011 *Comput. Phys. Commun.* **182** 1708–20
[34] Graf T, Casper F, Winterlik J, Balke B, Fecher G H, Felser C and Anorg Z 2009 *Allg. Chem.* **635** 976–81
[35] Alijani V, Ouardi S, Fecher G H, Winterlik J, Naghavi S S, Kozina X, Stryganyuk G, Felser C, Ikenaga E and Yamashita Y 2011 *Phys. Rev. B: Condens. Matter Mater. Phys.* **84** 224416
[36] Wang X, Cheng Z, Liu G, Dai X, Khenata R, Wang L and Bouhemadou A 2017 *IUCrJ* **4** 758–68
[37] Nepal S, Dhakal R, Galanakis I, Winter S M, Adhikari R P and Kaphle G C 2022 *Phys. Rev. Materials* **6** 114407
[38] Born M and Huang K 1956 *Dynamical Theory of Crystal Lattices* (Clarendon)
[39] Bounab S and Bentabet A 2023 *Indian J. Phys.* **97** 1389–95
[40] Voigt W 1910 *Lehrbuch der kristallphysik*:(*mit ausschluss der kristalloptik*) 34 (*BG Teubner*)
[41] Reuss A 1929 *J. Appl. Math. Mech.* **9** 49
[42] Hill R 1952 *Proc. Phys. Soc., Sect.* A **65** 349
[43] Hill R 1963 *J. Mech. Phys. Solids* **11** 357
[44] Pugh S 1954 *The London, Edinburgh, and Dublin Philosophical Magazine and Journal of Science* **45** 823
[45] Iyigor A and Ugur S 2014 *Philos. Mag. Lett.* **94** 708
[46] Wu S-C, Fecher G H, Shahab Naghavi S and Felser C 2019 *J. Appl. Phys.* **125** 082523
[47] Pettifor D G 1992 *Mater. Sci. Technol.* **8** 345
[48] Born M and Huang K 1954 *Dynamical Theory of Crystal Lattices* (Oxford University Press)
[49] Manzoor M, Behera D, Sharma R, Iqbal M W, Mukherjee S K, Khenata R, Alarfaji S S and Alzahrani H A 2023 *Mater. Today Commun.* **34** 105053
[50] Ravindran P, Fast L, Korzhavyi P A and Johansson B 1998 *J. Appl. Phys.* **84** 4891
[51] Ranganathan S I and Ostoja-Starzewski M 2008 *Phys. Rev. Lett.* **101** 55504
[52] Nye J F 1985 *Properties of Crystals* (Oxford University Press)
[53] Ozdogan K, Şaşıoğlu E and Galanakis I 2013 *J. Appl. Phys.* **113** 193903
[54] Dhakal R, Nepal S, Galanakis I, Adhikari R P and Kaphle G C 2021 *J. Alloys Cmpd.* 160500
[55] Dhakal R, Nepal S, Ray R, Paudel R and Kaphle G 2020 *J. Magn. Magn. Mater.* **503** 166588
[56] Nepal S, Dhakal R and Galanakis I 2020 *Mater. Today Commun.* **25** 101498
[57] Mazin I I 1999 *Phys. Rev. Lett.* **83** 1427–30
[58] Smith N V 1971 *Phys. Rev.* B **3** 1862
[59] Shan W, Walukiewicz W, Ager III J W, Haller E E, Geisz J F, Friedman D J, Olson J M and Kurtz S R 1999 *Phys. Rev. Lett.* **82** 1221
[60] Penn D R 1962 *Phys. Rev.* B **128** 2093
[61] Khoshman J M, Jakkala P, Ingram D C, Kordesch M E and NonCryst J 2016 *Solids* **31** 440
[62] Bakhshayeshi A, Sarmazdeh M M, Mendi R T and Boochani A 2017 *J. Electron. Mater* **46** 2196
[63] Goldsmid H J and Douglas R W 1954 *J. Appl. Phys.* **5** 386
[64] Tritt T M 2011 *Rev. Mater. Res.* **41** 433–48
[65] Slack G A 1979 *Solid State Phys.* **34** 1
[66] Morelli D T, Jovovic V and Heremans J P 2008 *Phys. Rev. Lett.* **101** 035901
[67] Blanco M A, Francisco E and Luania V 2004 *Comput. Phys. Commun.* **158** 57–72
[68] Yaseen M, Shafiq H, Iqbal J, Misbah, Batool F, Murtaza A, Iqbal M, Althib H, Ramay S M and Mahmood A 2021 *Physica* B **612** 412626

[69] Shukla P, Tiwari S, Joshi S R, Akshay V R, Vasundhara M, Varma S, Singh J and Chanda A 2018 *Physica* B **550** 303–10
[70] Xiong L, Yi L and Gao G Y 2014 Search for half-metallic magnets with large half-metallic gaps in the quaternary Heusler alloys CoFeTiZ and CoFeVZ (Z=Al, Ga, Si, Ge, As, Sb) *J. Magn. Magn. Mater.* **360** 98–103
[71] Khandy S A and Chai J-D 2020 Thermoelectric properties, phonon, and mechanical stability of new half-metallic quaternary Heusler alloys: FeRhCrZ (Z = Si and Ge) *J. Appl. Phys.* **127** 165102
[72] Liu J-R, Wei X-P, Chang W-L and Tao X 2022 Structural stability, electronic, magnetic and thermoelectric properties for half-metallic quaternary Heusler alloys CrLaCoZ *J. Phys. Chem. Solids* **163** 110600
[73] Mudassir Ishfaq M Y and Shazia Shukrullah S N 2024 Optoelectronic and thermoelectric transport phenomena in Sr2LaTaO6 and Sr2LuTaO6 double perovskites *Mater. Chem. Phys.* **313** 128728
[74] Ma H, Yang C-L, Wang M-S, Ma X-G and Yi Y-G 2019 *J. Phys. D: Appl. Phys.* **52** 255501
[75] Nazar M, Nasarullah, Aldaghfag S A, Yaseen M, Ishfaq M, Khera R A, Noreen S and Abdellattif M H 2022 *J. Phys. Chem. Solids* **166** 110719
[76] Ghellab T, Baaziz H, Charifi Z, Telfah M, Alsaad A, Telfah A, Hergenroder R and Sabirianov R 2022 *Mater. Sci. Semicond. Process.* **141** 106415
[77] Ghellab T, Baaziz H, Charifi Z, Bouferrache K, Saeed M A and Telfah A 2019 *Mater. Res. Express* **6** 075906
[78] Ghellab T, Baaziz H, Charifi Z, Bouferrache K, Uğur Ş, Uğurand G and Ünver H 2019 *Int. J. Mod. Phys.* B **33** 1950234
[79] Mili I, Latelli H, Ghellab T, Charifi Z, Baaziz H and Soyalp F 2021 *Int. J. Mod. Phys.* B **35** 2150100
[80] Telfah A, Ghellab T, Baaziz H, Charifi Z, Alsaad A M and Sabirianov R 2022 *J. Magn. Magn. Mater.* **562** 169822
[81] Charifi Z, Ghellab T, Baaziz H and Soyalp F 2022 *Int. J. Energy Res.* **46** 13855–73
[82] Ghellab T, Baaziz H, Charifi Z and Latelli H 2023 *Physica* B **653** 414678
[83] Mekki H, Baaziz H, Charifi Z, Ghellab T, Genç A E, Uğur Ş and Uğur G 2023 *Solid State Commun.* **363** 115103
[84] Kazim M Z, Yaseen M, Ghaffar A and Bhatti I A 2023 *Arab. J. Sci. Eng.* **48** 779–87